

The Geometry behind the Two-Dimensional Hard-Disk ‘Glass Transition’

J. de Graaf^{1,*}

¹*Institute for Theoretical Physics, Center for Extreme Matter and Emergent Phenomena,
Utrecht University, Princetonplein 5, 3584 CC Utrecht, The Netherlands*

(Dated: November 5, 2024)

The relation between dynamics and structure in systems of bidisperse 2D hard disks with apparent arrested dynamics is considered using numerical simulations and Voronoi analysis. Surprisingly, the suspensions systematically appear to fall out of equilibrium at an area fraction of $\phi \approx 0.777$ over a wide range of disk-size ratios. This is in close agreement with the experimental findings of [Lozano *et al.*, Nat. Mater. **18**, 1118 (2019)] for a single large-to-small size ratio of ≈ 1.4 . Even inside the crystalline region of the state diagram there are weak structural signatures present for this area fraction. Adopting a granocentric viewpoint, this allows for the identification of a geometric feature — a floret pentagonal tiling — that could underlie the observations. That is, this tiling has an area fraction of $\phi_g = \sqrt{3}\pi/7 \approx 0.777343$, which closely matches the apparent ‘glass transition’ value of ϕ . The connection suggests that a zero-entropy, ground-state tiling can influence the dynamics of the system at finite temperature, in a manner that may be similar to the way in which geometry in foam-like tissue models induces a jamming transition. A geometric ground-state argument also appears to explain the change in local dynamics observed by [Li *et al.*, Nature **587**, 225 (2020)], when a honeycomb lattice is used as the reference. Combined these findings change how to view high- ϕ 2D fluids, namely as being influenced by the presence of zero-entropy geometric ground states. The proposed connection leads to an unexpected (dynamic) transition in the finite-temperature system, which can be mistaken for a(n onset) glass transition, but is in a class of its own. There is also a tentative connection to random loose packing for frictional systems. An outlook is provided on how this concept may be extended to soft-particle systems and into higher dimensions.

I. INTRODUCTION

Arrested dynamics in amorphous soft-matter systems has been a topic of significant interest for decades [3–9]. The experimental realization of colloidal glasses made up of (almost) hard spheres [10–12], has given the field a strong impetus to consider the more fundamental question on the nature of the ‘glass transition’ [13]. In hard-particle systems, the glass transition takes place at a density for which the system exhibits a relaxation-time divergence [14], without its structure changing significantly from that of a fluid [15]. Despite the kinetic nature of this transition and a lack of obvious concurrent structural change, there has been a dedicated effort into obtaining structural signatures in experiment [16–19], simulation [20–25], and theory [26–28].

Over the years, structural signals have been found that correlate well with the appearance of slow dynamics at the particle-neighborhood and system level. For example, in three-dimensional (3D) glasses, such indicators are the abundance of icosahedral [29] or tetrahedral [30, 31] neighborhoods in the system. This type of research has recently taken flight with the application of machine learning [20, 32–42]. Machine learning appears able to identify subtle differences in local neighborhoods that correlate well with particle dynamics. Yet, these structural insights can be system dependent [43], and those obtained for 3D may not be (readily) transferrable to two-dimensional (2D) systems.

For 2D hard-disk suspensions and their quasi-2D equivalent — vertically confined hard-sphere systems — various local characterizations of a particle’s neighborhood have been considered. Such analyses typically start by Voronoi tessellating (or equivalently Delauney triangulating) realizations of the system [44–52]. Subsequently, features of the polygonal tiles are analyzed, *e.g.*, their aspect ratio [53], their anisotropy [54], the associated Minkowski tensor coefficients [55–57], *etc.* These studies have seen success in identifying the appearance of arrested dynamics, as well as the relation between structure and arrest, although frequently the result is subtle and the interpretation not entirely self-evident.

A. Experimental Inspiration and Open Question

Recently, however, an experimental study [1] revealed that self-propelled probe particles give a strong signal close to the ‘glass transition’ of hard spheres confined to a quasi-2D environment. That is, the orientation of the self-propelled probes is such that their rotational dynamics may be tracked and this changes upon varying the area fraction ϕ of the bidisperse hard-sphere mixture that surrounds it. The probe’s rotational diffusion D_p was found to be strongly enhanced with respect to its free ($\phi = 0$) value close to where the translational diffusion in the passive system drops off $\phi = \phi_g \approx 0.776$; even for small self-propulsion speeds. In addition, D_p was found to be peaked at ϕ_g and to decay asymmetrically away from its peak value as a function of ϕ . In Ref. [1], this observation was related to the increase in the bulk

* j.degraaf@uu.nl

relaxation time close to their ‘glass transition,’ using a theoretical model that incorporated a time-correlated reorientational noise based on the relaxation time.

It is important to note that in the experiments of Lozano *et al.* [1], the α relaxation times obtained from the self-intermediate scattering function follow the Vogel-Fulcher-Tammann (VTF) law [27, 58] exceptionally well. The VTF fit in Ref. [1] indicates a divergence at $\phi \approx 0.845$, which is close to where random close packing (rcp) for this colloid size ratio ($R \approx 1/1.4$) sets in, see also the ESI [59]. This seems to suggest that there is no glass transition at ϕ_g . Yet, the MSD curves in the experimental system do indicate a strong dynamical change close to ϕ_g . This was related to the system falling out of equilibrium and, hence, where the ‘glass transition’ is located.

Numerical modeling of the probe dynamics in the experimental system [60], performed in my group showed that an asymmetric peak D_p can be obtained using a contact-based friction that induces reorientation. However, it proved difficult to place the peak value close to the experimentally observed $\phi_g \approx 0.776$. The D_p peaks were systematically located closer to the ϕ value associated with rcp. We speculated that this may be attributed to a lack of dissipative interactions, such as contact friction or lubrication, that we did not account for in our modeling of the passive fluid. Thus, while our simple model was able to produce qualitatively the features observed in experiment, there remained an open question as to the nature of the ‘glass transition’ in this system.

This study was followed up by an experimental and numerical work on a quasi-2D system of colloidal rods [61], which was initiated in the Bechinger group and where my group provided the numerical modeling. Together, we revealed that there is a D_p enhancement for spherical self-propelled probes close to the glass transition, which is well captured using the reorientation model of Ref. [60]. In addition, we found that only considering the passive (thermal) rod particles is sufficient to accurately predict the enhancement, meaning that the probes pick up on local features present in the passive system alone. More intriguingly, there was a visually evident structural change in the system close to ϕ_g , namely the breaking up of large rafts of colloidal rods into smaller clusters [61].

B. Dual Goal of the Study

Both the difficulty in reproducing numerically the experimental ‘glass transition’ in Ref. [60] and the presence of an apparent structural signal for enhancement in the rod-like systems [61], suggest that it is worth revisiting the quasi-2D hard-sphere system of Ref. [1]. One aim of this work is therefore to identify structural features that correlate with (the onset of) arrested dynamics and thereby understand the origin of the observed ϕ_g .

Given the prevalence of Voronoi-based analysis in (effective) 2D modeling, I will follow a tessellation-based analysis route. However, I additionally draw inspira-

tion from the adjacent field of epithelial tissue modeling, in particular, foam-like vertex- and Voronoi-based approaches [62–69]. When there are N cells, these systems typically possess a Hamiltonian of the form

$$\mathcal{H} = \sum_{i=1}^N \left[\kappa_A (A_i - A_0)^2 + \kappa_P (P_i - P_0)^2 \right], \quad (1)$$

where A_i and P_i are the instantaneous area and perimeter length of the i -th (Voronoi) cell, respectively. The parameter A_0 is the target area and P_0 represents the target perimeter length, which are the rest ‘sizes’ for the harmonic terms in the Hamiltonian. Note that these target shape parameters are common to all cells.

It is well-established that there is a transition from an amorphous fluid-like state to an amorphous solid-like state when the shape index $p_0 \equiv P_0/\sqrt{A_0} = p_0^* \approx 3.81$ [62, 63]. The transition shape index p_0^* is identical to that of a regular pentagon — a 5-sided polygon for which all edges and angles are equal. The physical intuition is that this choice of p_0 leads to frustration, since regular pentagons do not tessellate space. That is, there is a mismatch between the local requirement on the cells to be pentagonal and the global requirement on the model epithelium to be confluent (cover all of space).

Bi *et al.* [62] showed that the onset of arrested dynamics — here referred to as a jamming transition as the system need not be thermal [70] — can be correlated to the appearance of a barrier that hinders topological exchange between neighboring cells. The second aim of this work is to extend these ideas to hard-particle systems and what insight they can provide into the structural origin of the reported ‘glass transition’ [1].

C. Approach and Result

I circumvent the issues in previously modeling the experimental system using soft potentials [60] by studying numerically 2D systems of hard disks using event-driven molecular dynamics (EDMD) simulations [71]. I focus on a stoichiometric ratio of 50:50 small to large disks, as in the experiment [1], but I also analyze a far larger range of size ratios $R \in [1/1.7, 1]$ and area fractions ϕ . Here, R is the ratio of the small to the large disk diameter. For these systems, I determine the radical Voronoi diagram [50] and show how to use the statistics of the particle neighborhoods to obtain a state diagram. I base these statistics on the isoperimetric quotient q , which is a variant of the aforementioned shape index p ($q = 4\pi/p^2$).

Using the mean of q , I can determine when the system crystallizes, which occurs when the average shape is that of a 5.5-gon. I will introduce how to define the isoperimetric quotient of a polygon with a non-integer number of edges and show how this reveals a re-entrant amorphous state as ϕ is increased at a sufficiently low value of R . In fact, my state diagram appears to have a ‘critical point’ in R and ϕ , which correlates well with the

system falling out of equilibrium. Although the analogy should not be taken too far, given that above the ‘glass transition’ the system is slow to equilibrate.

Surprisingly, I find that for $R \lesssim 0.83$ the area fraction, for which the particle dynamics appears to become arrested, is nearly constant $\phi \approx 0.777$. I confirm this measurement, which is based on the mean squared displacement (MSD), by examining features in a shell-based percolation measure. A small feature in the amount of pentagonal neighborhoods for the *large* particles in the systems tracks this arrested-dynamics line very well. Unexpectedly, this even extends the line $\phi \approx 0.777$ into the region where the system crystallizes, which includes monodisperse systems. I analyze the established literature on structure and dynamics in 2D systems in detail and find hints in several theory and simulation papers that support my finding of a constant- ϕ behavior.

The fact that non-equilibrium features are present in the otherwise crystalline monodisperse system, inspired me to adopt a granocentric viewpoint. That is, I consider the properties of a neighborhood around a single disk in an otherwise monodisperse system. This allows me to identify a convex pentagonal shape for the Voronoi cell around this disk, when it is in contact with 5 neighbors. The configuration has a local area fraction $\phi_g = \sqrt{3}\pi/7 \approx 0.777343$. Interestingly, this shape may be assembled into a floret pentagonal tiling [72, 73], which is a known way to tile space with congruent pentagonal elements. In this particle organization, each disk is in direct contact with 5 neighbors, which makes it a local entropic minimum with both zero configurational and vibrational entropy.

D. Conclusion

The combined body of evidence that I present, allows me to propose an unexpected origin of the ‘glassy dynamics’ in the considered system. Namely, the pentagonal-floret tiling is a zero-entropy ‘geometric ground state’, wherein every particle is completely immobilized. The presence of this ground state echoes through in the disordered fluid, in a similar fashion as setting the shape index in a foam-like tissue model. That is, the floret pentagonal tiling enforces the slow dynamics at $\phi_a \approx 0.777$, thereby localizing what is identified as a ‘glass transition’ in the original experiment [1]. I also provide tentative evidence that the onset of caging in the system can be viewed in a similar fashion. I propose that it is related to a honeycomb-lattice geometric ground state and make the connection to the experimental work by Li *et al.* [2].

The crux to this understanding lies in moving away from the idea that (2D) fluids are disordered systems. Instead, at least at sufficiently high density, these should be considered as entangled with ordered low-entropy ground states that can enforce geometric frustration even at finite temperature. The rapid change in dynamics observed in experiment, as well as the response behavior when subjected to active and/or external probing [1, 2],

is then not because of subtle changes in the structure of the fluid. Instead, it is caused by radical changes in the entropy of the entangling (reference) geometric ground state. I will also provide arguments to support this viewpoint, although within the scope of this work, I was unable to come to a full theoretical understanding.

E. Structure of the Paper

The remainder of this paper is organized as follows. Section II provides the details necessary to reproduce my results and Section III the ways, in which I characterized the structure in the bidisperse hard-disk system. The major features of working with the isoperimetric quotient are put forward in Section IV, which is followed by an analysis of the dynamics in the system *via* the MSD in Section V. Together, these results lead me to propose a state diagram in Section VI, which is discussed in detail. Next, I correlate structural features to particle dynamics in Section VII, which is supplemented by a literature analysis (Appendix A). Then, I present my geometric model and understanding in Section VIII. The implications of the study are further contextualized in the discussion, where I also give a perspective on an extension to 3D, see Section IX and Appendix F. Lastly, I provide a short summary of the work in Section X.

II. SYSTEM AND NUMERICAL APPROACH

I study structural and kinetic properties of systems of binary hard disks in 2D using the EDMD software developed by Smallenburg [71]. The algorithms were appropriately modified for use in 2D, see the ESI [59]. In this variant of EDMD, the system is thermalized and maintained at a reduced temperature of $T = 1$. The choice of parameters is such that in the limit of $\phi \downarrow 0$ the diffusion coefficient of the particles is given by $D = 1$. That is, the reduced time is expressed in the diffusion time.

The investigated systems consist of a 50:50 mixture of small and large discs, for which two particles (indexed i and j) interact *via* the pair-interaction potential

$$U(r) = \begin{cases} 0 & 2r > \sigma_i + \sigma_j \\ \infty & 2r \leq \sigma_i + \sigma_j \end{cases}, \quad (2)$$

where r measures the center-to-center distance and σ_i and σ_j are the respective particle diameters. I will refer to the diameter of the largest particles as σ and write the diameter of the small particles as $R\sigma$, with $R \leq 1$ the diameter ratio. Throughout this paper, I will flexibly label graphs by either R or R^{-1} , where the latter is often a more precise notation because of parameter choices made in my study. That is, $R^{-1} = 1.7$ has a preference over the notation $R \approx 0.5882352941 \dots$.

In all cases, I simulated $N = 2,048$ particles in a square simulation box with edge length L and periodic boundary conditions [74]. The value of L was varied such that I

could simulate area fractions $\phi = (\pi/8)\sigma^2 (1 + R^2) N/L^2$ between 0 and ϕ_m . The latter is the random-close packing (rcp) area fraction, ϕ_m . I established ϕ_m for a given R using the approach of Desmond and Weeks [75], the limitations of which are discussed in Appendix A. In brief, I computed 250 potential (random) closest packings using the same number of particles N as employed for my production runs. I then selected the highest value of ϕ and thus obtained the rcp area fraction ϕ_m as a function of R , see Section VI for the result.

I typically considered 100+ non-equidistant points $\phi \in [0, \phi_m]$ for each value of R . For each R - ϕ combination, I then generated 150 independent realizations of the system by slowly growing the particles until the target value of ϕ had been obtained, see the ESI [59]. A dimensionless growth rate of 10^{-3} proved sufficient to obtain initial configurations for all ϕ even very close to ϕ_m . It should be noted, however, that the time for finding an initial configuration increased substantially as $\phi \uparrow \phi_m$, which is expected for the highly constrained packing.

Next, I allowed each configuration to evolve for 10^4 reduced time units without growth, before I started to sample. As we will see, there are slow dynamics in the system and 10^4 time units may be too short of a time to fully equilibrate the system for all considered ϕ - R combinations. Here, I focused on removing any bias that could be present in the system at low to intermediate ϕ by creating the configurations *via* growth. The 150 configurations per R - ϕ point were used to obtain error bars and relatively accurate statistics.

Lastly, for the purposes of completeness, I should note that in addition to EDMD [71], I have attempted to create and equilibrate systems using plain Metropolis, rejection-free [76, 77], and swap variants of the Monte Carlo algorithm [21, 78, 79]. However, none of these methods proved to be more efficient than the EDMD algorithm used here. In particular, the use of swap Monte Carlo proved challenging, due to the bidisperse hard-particle nature of the sample at small values of R . That is, most moves were rejected beyond a certain value of ϕ . Though, I should note that by no means this implies that these algorithms are not generally useful to study hard-particle systems with arrested kinetics, for example, as recently evidenced in Ref. [80].

III. CHARACTERIZATION

The purpose of this paper is to probe the connection between arrested dynamics and isoperimetric properties of the local particle neighborhoods. I therefore compute the radical Voronoi tessellation (also known as power diagram or Dirichlet cell complex) using the `voronoi++` library [81, 82]. The radical Voronoi tessellation respects the radius difference between the two sizes of particles in the system. Figure 1a shows a result of this analysis for a small part of a simulation volume in for $R^{-1} = 1.4$ at an area fraction of $\phi = 0.777$; close to the experimental

value for the glass transition [1].

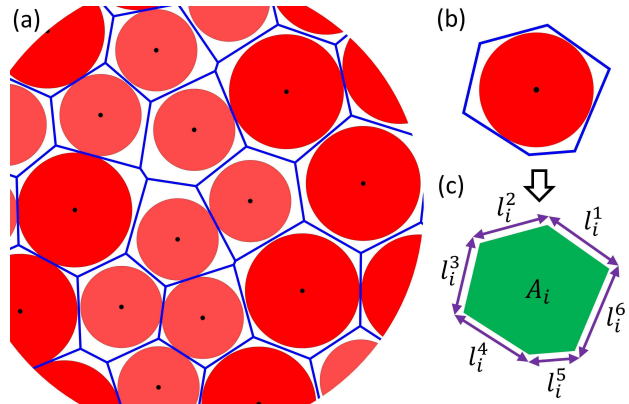


FIG. 1. **Procedure for computing the isoperimetric quotient using a Voronoi tessellation.** (a) Part of a snapshot of a system showing the instantaneous organization of bidisperse disks with size ratio $R^{-1} = 1.4$ at an area fraction of $\phi = 0.777$. The smaller disks are indicated in light red, while the larger disks are in the darker shade of red. The centers of the disks are indicated using black dots and the blue lines surrounding the disks represent the radical Voronoi diagram for the system. Note that none of the disks overlap though this is hard to resolve by eye. (b) An example of a Voronoi cell for a large particle which has 6 sides, which is the i -th cell in this sample. (c) The area A_i of this cell (green) together with the perimeter length $P_i = \sum_n l_i^n$ (purple arrows) are used to compute the isoperimetric quotient $q_i = 4\pi A_i / P_i^2$.

Using the Voronoi cells obtained in this manner, I compute the isoperimetric quotient

$$q = \frac{4\pi A}{P^2}, \quad (3)$$

for each particle, where A is the area of the associated Voronoi neighborhood and P is its perimeter. Note that $q \in (0, 1]$, where $q = 0$ corresponds to an extremely needle-like Voronoi neighborhood, while $q = 1$ represents a perfect circle. Recall that for each R - ϕ combination, there are $150 \times 2,048$ q values. This allows me to compute using non-linear binning the probability density function for q , here denoted $P_\phi(q)$, to a high degree of accuracy, as I will present in Section IV.

The distribution $P_\phi(q)$ is insightful, but to help understand the properties of the underlying system, it is beneficial to convert q to an effective number of vertices n_q [83]. The isoperimetric quotient of regular polygons with n edges can be readily computed and reads

$$q_r(n) = \frac{4\pi A_r(n)}{P_r^2(n)} = \frac{\pi \sin(2\pi/n)}{2n \sin^2(\pi/n)}, \quad (4)$$

where $A_r(n)$ and $P_r(n)$ are the area and the perimeter of a regular polygon having n edges and a circumscribing circle with radius $r = 1$. This function maps the number of the edges of regular polygons to their isoperimetric quotient and *vice versa*. The right-hand side of Eq. (4)

can now straightforwardly be applied to non-integer values of n . I introduce the concept of a *generalized number of edges* to underscore that non-integer values are permissible, such as $n = 5.2$. In addition, I make use of the subscript ‘ q ’ to indicate the origin of this number: n_q .

Numerically inverting Eq. (4), I am able to obtain an n_q for any value of q . Note that there is only a single polyhedron that maps to integer values of n_q , namely the regular one. However, there are many, subtly different polyhedra that give, for example, the value $n_q = 5.2$. The point of introducing the generalized number of edges is to see all of these as roughly the same and close to pentagonal, as already though less clearly expressed by q . The definition of n_q also allows me to identify ranges in q that intuitively correspond to certain polygons [83]. That is, I assign a specific value of n_q to belong to triangular, square, pentagonal, hexagonal, heptagonal, *etc.* neighborhoods by taking $\lfloor n_q \rfloor$. This choice factors the n_q (equivalently q) range into distinct subsets n -fold pseudo polygons. For example, all neighborhoods having $\lfloor n_q \rfloor = 5$ (*i.e.*, $4.5 < n_q \leq 5.5$) can be referred to as *pseudo-pentagons*. Integrating the PDF belonging to the pseudo-pentagons provides insight into the fraction of pentagonal neighborhoods in the system, also see Appendix B. This includes neighborhoods with more than five edges, for which some edges are very small and therefore the neighborhood has the appearance of a pentagon, Fig. 1 shows several examples of this.

I also computed several ensemble-averaged and time-dependent physical quantities of interest to further support my arguments. These include the pressure p , see Appendix C, and two variants of cluster percolation, see Appendix D. Lastly, I determined the kinetics in the bidisperse hard-disk samples by computing the MSD. I obtained particle displacements for 10^4 unit times starting from the ‘equilibrated’ samples. These were averaged in time, which led to 150 MSD curves that were also averaged over all particles in the system. Subsequently, I determined the mean of the independent MSD data — the initial configuration varies — as well as the associated standard deviation. Section V provides additional details on the processing of this data, by which I obtained the area fraction ϕ_a for which arrested dynamics sets in.

IV. NEIGHBORHOOD STRUCTURE

Now let us turn to the outcome of my structural characterization. Figure 2a-c shows a sampling of the isoperimetric-quotient PDFs, $P_\phi(q)$, for three values of R and 6 values of ϕ , as labelled. Note that irrespective of R , the low- ϕ diagram is similar. The distribution tends to an established curve as $\phi \downarrow 0$ that was computed for Voronoi diagrams deriving from uniformly distributed points [84, 85]. This makes sense, as for low ϕ , properties such as differences in particle size should wash out of the distributions, as also seen in the literature [86].

The results become more interesting when examining

intermediate to high values of ϕ . Note there are discontinuities in the slope of $P_\phi(q)$ at specific values of q . The q values correspond to those of a regular n -gon — $q_r(n)$ in Eq. (4) — as is illustrated using the vertical black lines in Fig. 2. This is *not* a profound result and can be easily explained as follows. Any polygon with a number of sides less or equal to say 5 can only contribute to $P_\phi(q)$ for $q \leq q_r(5)$. However, there are also hexagonal, heptagonal, *etc.* neighborhoods that appear pentagonal, but for which $q \gtrsim q_r(5)$. As it is statistically unlikely to have regular pentagons in the sample, this gives rise to a dip in $P_\phi(q)$ and an associated slope discontinuity.

Comparing the high- ϕ PDFs for the three R values, I observe that the monodisperse ($R = 1$) system convincingly crystallizes. The PDF has a single peak which is close to $q_r(6)$, as expected. For lower values of R , there remains a sizable fraction of pentagons and there can also be a significant number of heptagons, when R is sufficiently small. I refer to Appendix B for additional details on the fraction of pseudo-polygons. For systems with $R^{-1} \gtrsim 1.4$, I consistently find that the two peaks in the ranges $(q_r(4), q_r(5)]$ and $(q_r(5), q_r(6)]$ are comparable in height. However, there is a slight abundance of pseudo-pentagons, see Appendix B. This means that the disk configurations are not crystalline.

The features of the $P_\phi(q)$ will be further analyzed in Section VII. However, before turning to dynamics in Section V, I will first consider the mean value of q that can be obtained from $P_\phi(q)$ by taking the first mode of the distribution. Let this be denoted by \bar{q} and its associated generalized number of edges by $n_{\bar{q}}$. The latter is shown as a function of ϕ in Fig. 2d for all values of R considered. The curves are generally smooth within the error. There is no apparent gap or discontinuity for those systems that are known to undergo a phase transition. This is because I worked in the constant area, particle, and temperature ensemble. There appears to be a change in slope close to where the system is expected to crystallize (for $R \lesssim 1$), but I did not investigate this further. The generalized number of edges $n_{\bar{q}}$ is an increasing function of ϕ for $\phi \lesssim 0.76$. For greater area fractions, I find a single, well-defined maximum, beyond which $n_{\bar{q}}$ decreases rapidly. I will use this feature, as well as the intersection points with $n_{\bar{q}} = 5.5$, see inset to Fig. 2d, in preparing a R - ϕ state diagram in Section VI.

V. PARTICLE DYNAMICS

Let us now consider the dynamics in the systems. As explained in Section III, I obtained MSDs for a range of ϕ given a specific value of R . That is, I computed $\langle |\mathbf{r}(t)|^2 \rangle$, where \mathbf{r} is an individual particle’s displacement from (reduced) time $t = 0$ and the angular brackets indicate ensemble averaging. Figure 3a provides examples of such MSD data for $R^{-1} = 1.45$, which is close to the experimental R value of Ref. [1] and also a representative sample for the other R considered in this work. Data for

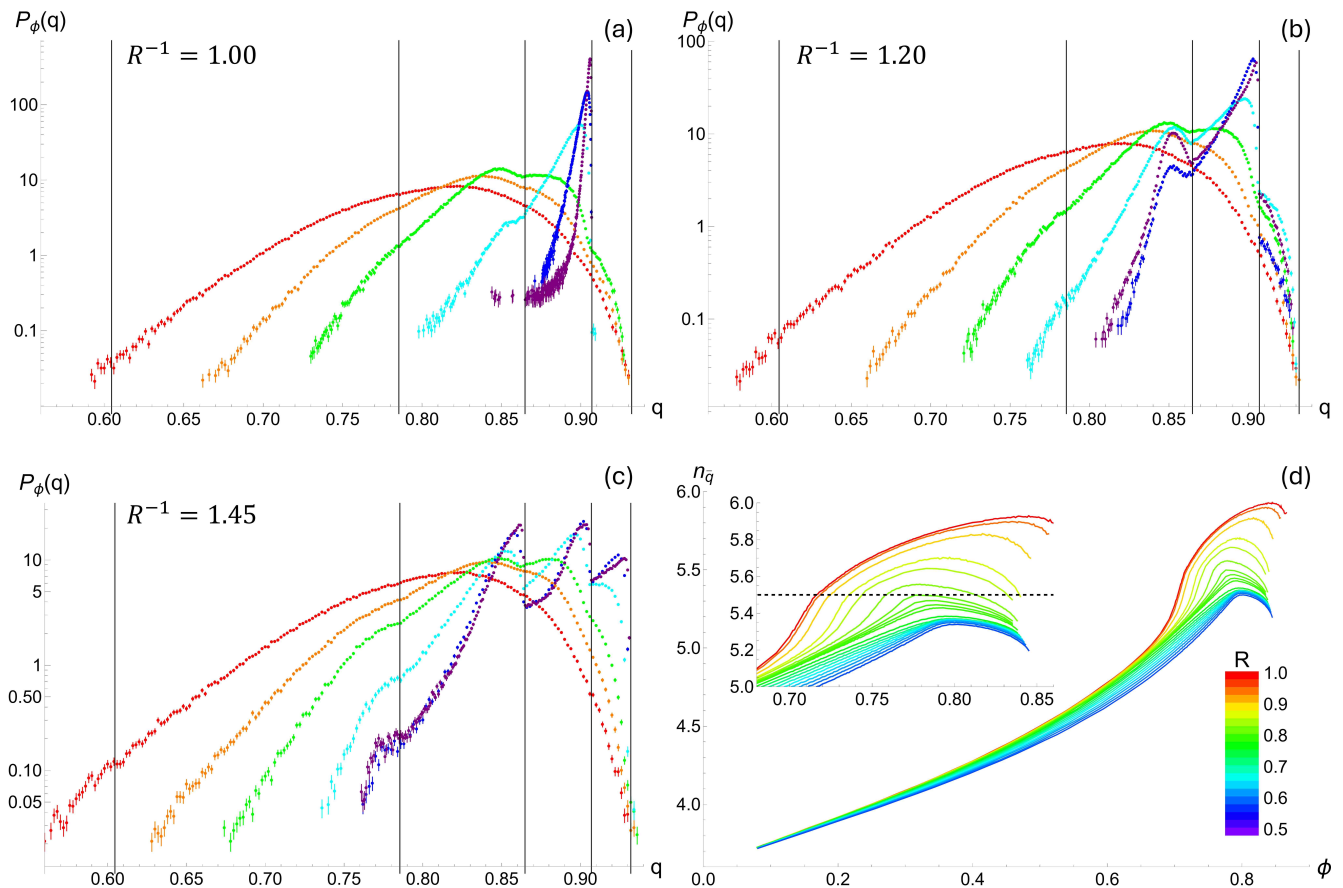


FIG. 2. **Structural features of the 2D system characterized by the isoperimetric quotient.** (a-c) The probability density function (PDF) $P_\phi(q)$ of the isoperimetric quotient q for several values of the area fraction ϕ in lin-log representation. The inverse size ratio R^{-1} between the large and small spheres in the system is provided in by the label. From red to purple, the area fractions are $\phi = 0.350$ (red), 0.500 (orange), 0.610 (green), 0.720 (cyan), 0.780 (blue), 0.825 (purple), respectively. The vertical black lines provide the q values for a regular n -gon, with $n = 3, \dots, 7$ from left to right. The error bars indicate the standard deviation on the binned value for the interval over which $P_\phi(q)$ is sampled, which adheres to counting statistics and is thus always the square root of the number of samples in a bin. (d) The generalized number of edges $n_{\bar{q}}$ belonging to the mean q value — \bar{q} : the first moment of $P_\phi(q)$ — as a function of ϕ for all size ratios R considered. From red to purple the value of the size ratio is given by $R^{-1} = 1.00, 1.05, 1.10, 1.15, 1.17, 1.20, 1.22, 1.23, 1.24, 1.25, 1.30, 1.35, 1.40, 1.45, 1.50, 1.55, 1.60, 1.65,$ and 1.70, respectively. The inset shows a zoom-in on the range where the systems form crystals, *i.e.*, above the dashed horizontal line provides the value $n_{\bar{q}} = 5.5$. I do not provide error bars here to help improve the representation. The error is about twice the line width, as can be appreciated from the noise that is present on the red curve in the inset.

which the standard error exceeds 5% of the mean on the last point is not shown. However, it should be noted that data for values of $\phi > 0.744$ was studied and that within the error in this data, I observe a plateau to the MSD, which is indicative of strong caging.

From the selected curves, I extracted the power-law coefficient α that best described the long-time behavior of the MSD, *i.e.*, $\langle |r|^2 \rangle \propto t^\alpha$. The ESI [59] provides full details on the procedure. Whenever this fitting procedure led to an $\alpha \in (0.97, 1]$, I used the fit to also obtain the effective, reduced diffusion coefficient D . As expected, D decreased as a function of ϕ , see Fig. 3b. It was found to exhibit power-law decay close to the point where D became vanishingly small. Beyond the associated ϕ value, the MSD also typically started to become significantly

subdiffusive (not shown here).

I fitted the diffusive, power-law decaying part of the MSD using a variable-exponent power law $A(\phi_a - \phi)^b$, where A is a prefactor, b the exponent, and ϕ_a the area fraction for which the extrapolated dynamics becomes arrested. The value of b was found to increase from ≈ 0.7 at $R = 1$ to ≈ 1.3 for $R = 0.8$. Attempts to obtain b for $R < 0.8$ led to data with significant and undesirable level of scatter in b (though the associated ϕ_a were less scattered). I therefore fitted with a value of $b = 1.3$ below the size ratio $R = 0.8$. Referring forward to Section VI the idea behind this choice is that once the system no longer crystallizes, the exponent b freezes out.

My approach can raise questions regarding the quality of the fit and precision with which I obtained ϕ_a , as well

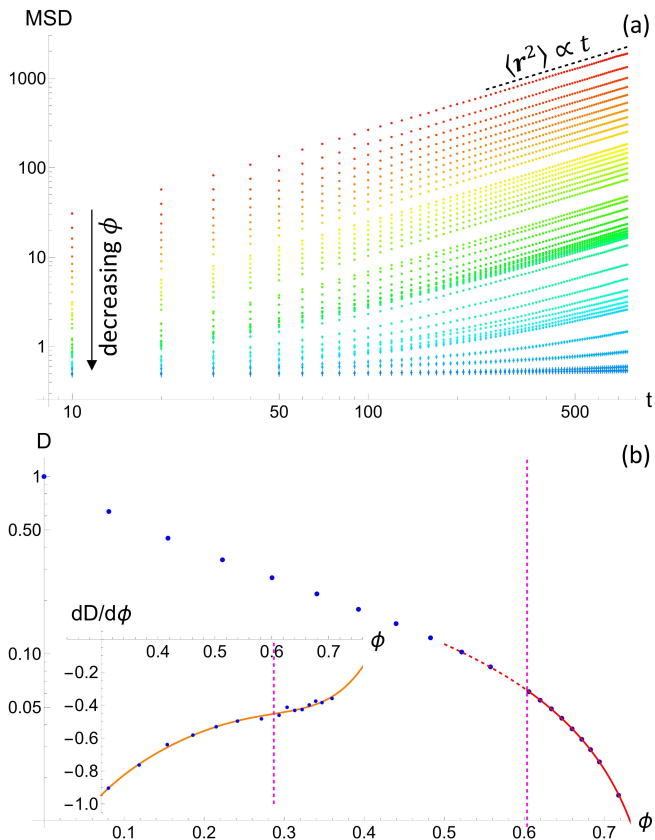


FIG. 3. **Analyzing the dynamics in the system.** All the data in this set of graphs was obtained for $R^{-1} = 1.45$. (a) The reduced mean squared displacement (MSD) as a function of the reduced time t . From red to blue the value of the area fraction ϕ decreases from 0.081, 0.155, 0.223, 0.285, 0.341, 0.393, 0.44, 0.483, 0.522, 0.558, 0.606, 0.62, 0.634, 0.647, 0.66, 0.672, 0.683, 0.694, 0.718, 0.723, 0.731, 0.739, to 0.744, respectively. The dots show the average and the error bars the standard error of the mean. The dashed black line shows the linear scaling of the MSD for large times. (b) Logarithmic plot of the reduced diffusion coefficient D as a function of ϕ for the data in (a). The error is typically much smaller than the symbol size. The red curve shows a power-law fit to the data. The vertical dashed vertical magenta line indicates the inflection point to the change in diffusion. The inset shows the numerical derivative $\partial D/\partial\phi$ as a function of ϕ . The solid orange curve shows a quintic polynomial fit to this data and the magenta line is the same as in the main panel.

as its sensitivity to the procedure of preparing the systems. To address the first of these concerns, I approached finding ϕ_a using structural characteristics as well, see Appendix D, wherein I use shell percolation [87]. In brief, there is a small, but measurable feature in the way the shell-percolation point changes with the shell width ϵ as a function of ϕ . I found excellent agreement between the ϕ for which this feature appears and ϕ_a , in the range where ϕ_a was observed to be nearly constant. Here, I should emphasize that arrested dynamics, as identified through ϕ_a , is not necessarily indicative of glassy dynamics. It

may equally result from the system crystallizing or undergoing another type of phase transition, as will become clear in Section VI.

Turning to the second point, it is not clear that the value of ϕ_a is insensitive to equilibration and preparation. I address this issue by performing simulations with equilibration lengths ranging from 10^3 and 10^5 reduced time units (post formation by growth) for several values of ϕ and R , see the ESI [59]. The changes across this time range to the structure were nominal. This provides confidence in my analysis of the dynamics and structure.

Having confirmed that the ϕ_a feature is robust to changes in equilibration time, I consider a final aspect of $D(\phi)$. Using a simple midpoint scheme, I numerically compute the derivative of D as a function of ϕ , see the inset to Fig. 3b. This data is fitted using a quintic polynomial (orange curve) and from this the inflection point to $\partial D/\partial\phi$ is obtained. I refer to the associated area fraction as ϕ_i and have indicated it in the inset using a vertical dashed magenta line. In the main panel (Fig. 3b), ϕ_i appears to be at the edge of where $D(\phi)$ decays slowly. I have suggestively indicated this by using dashing for the red curve to the left of the inflection point, though it should be noted that lin-log representations can be slightly deceptive in their interpretation. I will discuss the inflection-point data further in Section VII.

I close this section by mentioning that I have also briefly considered the decay present in the self-intermediate scattering function (SISF). It proved challenging to extract ϕ_a from the SISF data. Referencing the experiments of Lozano *et al.* [1] this is unsurprising. The relaxation times obtained from their SISF follow the Vogel-Fulcher-Tammann (VTF) law [27, 58] exceptionally well. This can be appreciated from their Fig. S3a and the re-analysis of their data in the ESI [59]. The area fraction for which the divergence occurs extracted from the VTF fit is $\phi \approx 0.845$, which is close to where I place the ϕ_m [88]. That is, the experimental data did not reveal a direct relation between properties of the SISF and the ‘glass transition’ that was observed. In view of this, I did not pursue further finding ϕ_a using the SISF, also because there were already two different approaches that gave good agreement for the value.

VI. STATE DIAGRAM

From my analysis of the rcp area fraction ϕ_m , the isoperimetric quotient q , and the diffusion coefficients D , I have put together an R - ϕ state diagram. This is shown in Fig. 4 and reveals the following trends.

The black points provide the ϕ_m upper bound for having a (disordered) system that is close packed. Note that for sufficiently high $R \approx 1$, the system is ordered and the notion of ‘random’ in rcp is abused, as snapshot 5 clearly reveals crystalline packing. The algorithm of Desmond and Weeks [75] itself does not check for a disordered structure, only for close packing, but I will

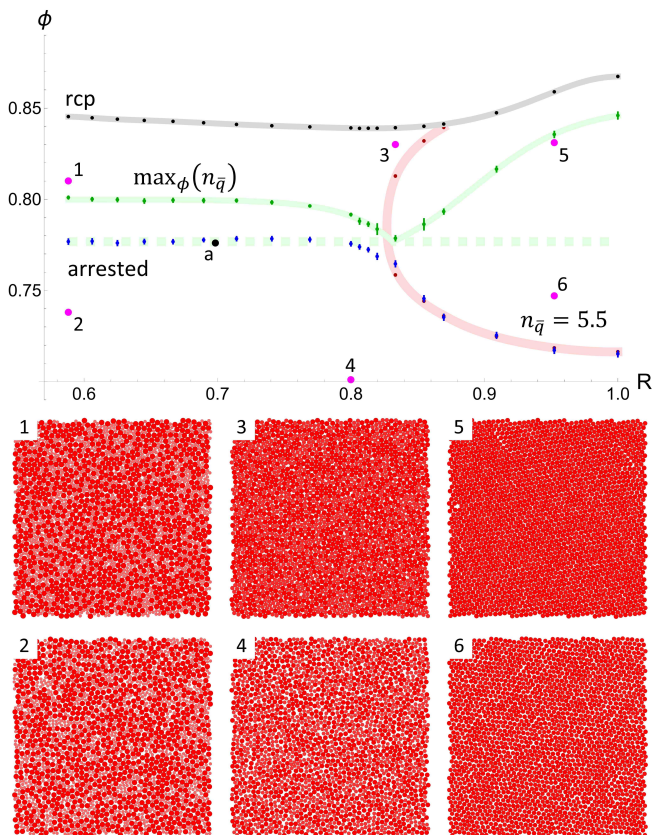


FIG. 4. **State diagram for bidisperse disks in 2D.** The data is represented in a size ratio R to area fraction ϕ diagram. Small dots with error bars provide the numerical data and the standard error of the mean, respectively. The solid curves provide guides to the eye for the trends. The black dots and light-black curve provide the random-close packing value, labelled ‘rcp’. The red dots and light-red curve shows those configurations for which the average generalized number of edges $n_{\bar{q}} = 5.5$. The red curve is thicker than the other ones, as there is more uncertainty as to what its shape is, see main text. The current representation involves a quartic fit near $R \approx 0.83$. The green dots and light-green curves show those systems, for which ϕ the value of $n_{\bar{q}}$ is maximized. The blue dots show the points for which the extrapolated dynamics is fully arrested, ϕ_a , as extracted from the mean-squared displacement, see Section III for the procedure. The horizontal, thick dashed, green line provides the value at which the systems fall out of equilibrium. The six numbered magenta dots correspond to the systems, for which I show a representative snapshot at the bottom of the figure, as labelled. In these snapshots the smaller disks are indicated using a lighter shade of red, which is related to the ratio R . The large black dot marked “a” indicates the glass-transition value $\phi = 0.776$ for $R \approx 0.7$ as obtained in the experiment of Ref. [1].

use it throughout, nonetheless. The light-black curve is a high-order polynomial fit to the data points and serves to guide the eye. The width of this (and other) curve(s) in the diagram corresponds roughly to the maximum deviation from the mean (standard error of the mean).

I correlate the presence of crystallinity throughout the

system with $n_{\bar{q}} > 5.5$; see Fig. 2d and its inset. For $R \gtrsim 0.83$ there are two intersection points for $n_{\bar{q}} = 5.5$, this leads to two distinct branches which must meet up in a single point. It proved difficult to find this point even for my fine-meshed R analysis, I therefore fit the data points closest to $R \approx 0.83$ using a polynomial containing a linear, square, and quartic term. This together with a polynomial fit of the data closer to $R = 1$, see the ESI [59], leads to the red envelope presented in Fig. 4. The curve for this envelope is thicker than that used for the other guides to the eye in the diagram, as there is more uncertainty on it, especially close to the ‘critical point’ in terms of R . Note that because there is low diffusivity above ϕ_a the analogy to an equilibrium critical point should not be taken too far.

Snapshots 5 and 6 reveal that the system is crystalline inside of this envelope, while snapshots 3 and 4 reveal disorder. Note that snapshot 3 has many crystalline areas in it, though the overall structure is clearly not that of an ordered solid. Analyzing the sample using $n_{\bar{q}}$ is thus useful to gain insight into bulk features. In Appendix C, I study the pressure as a function of ϕ . I use this to show that there is a reasonable agreement between the crystalline-phase coexistence density, as measured using the van-der-Waals loop, and the lower ϕ -branch that results from my (intuited) $n_{\bar{q}} = 5.5$ crystallization criterion. There is also satisfactory agreement with ϕ coexistence values previously reported in the literature for bidisperse hard-disk systems [89], given that my equilibration procedure is different from that of Huerta *et al.* This leads me to conclude that crystallization region is accurately located in the diagram.

Figure 4 also shows the value of ϕ , for which $n_{\bar{q}}$ assumes its maximum (green data). Note that the data clearly has two trends to it, which were individually fitted using a sigmoidal curve. This leads to the solid, light-green curve that also serves to guide the eye. Above $R \approx 0.83$, I find that $n_{\bar{q}}$ shows a descending trend with decreasing R . While below this value of R , $n_{\bar{q}}$ increases. Transition between these two regimes coincides with the closing of the $n_{\bar{q}} = 5.5$ (red) envelope within the error. The two trends are caused by the same effect. Above the ϕ value associated with $\max_{\phi}(n_{\bar{q}})$, the average neighborhood becomes increasingly anisotropic to accommodate the target area fraction. This could be caused by a global distortion of neighborhoods or by the incorporation of defects. I will provide additional evidence in Section VII.

For the systems that crystallize — within the $n_{\bar{q}} = 5.5$ envelope — the lower the value of R , the more freedom there is to distort neighborhoods, due to the presence of smaller particles. Thus, the value of ϕ for which distortion occurs, decreases with decreasing R . Outside of the envelope, the system is better characterized by disorder, which is occasionally interspersed with crystalline patches, see also snapshots 1, 2, and 4. Therefore, the smaller the value of R , the greater the area fraction must be to begin to see distortions in the neighborhoods of the small particles, which contribute 50% to the value of

$n_{\bar{q}}$. I also examined the ‘critical points’ that follow from the intersection of the green curves and from the peak (in R) of the red envelope, their location is $\phi \approx 0.777$ & $R^{-1} \approx 1.20$ and $\phi \approx 0.785$ & $R^{-1} \approx 1.21$, respectively. For $R \lesssim 0.83$, the system loses long-ranged orientational order, see the ESI [59], which leads to the change in trend.

I use the value of $\phi \approx 0.777$ as a tentative indication of where the system appears to fall out of equilibrium, as indicated using the dashed green line that covers the entire R range. I will motivate this extended range more carefully in the upcoming Section VII. Note that this value of ϕ is extremely close to what was reported for the experimental system of Lozano *et al.* [1], which found a ‘glass transition’ at $\phi \approx 0.776$ and $R \approx 0.70$.

Interestingly, when I analyze the value for which the (extrapolated) diffusion coefficient vanishes, ϕ_a , I find that this approaches $\phi = 0.777$ for sufficiently low R . That is, ϕ_a matches the constant dashed green curve well for $R \lesssim 0.8$ or equivalently $R^{-1} \gtrsim 1.25$. For $R \gtrsim 0.833$ ($R^{-1} \lesssim 1.2$), I further observe that ϕ_a accurately tracks the lower part of the red $n_{\bar{q}} = 5.5$ envelope. This makes sense, as diffusion in a crystal is mediated by interstitial mechanisms [90], which means that it is generally much slower than diffusion in a fluid. My fitting procedure for ϕ_a picks up on this difference in dynamics. The more surprising result is the near constancy of ϕ_a over a large range in R , which is what I will turn to next.

VII. STRUCTURAL SIGNALS OF CHANGES IN THE DYNAMICS

The fact that there is a relation between reduced dynamics and the $n_{\bar{q}} = 5.5$ data, inspired me to look for similar indicators of ϕ_a in the isoperimetric-quotient data for $R \lesssim 0.8$, where arrested dynamics appears to set in at nearly constant ϕ . In this section, I therefore consider the properties of the q distribution. I will also briefly comment on the inflection points to the dynamics that I introduced in Section V.

A. Large-Particle Pentagonal Neighborhoods

First, let us turn our attention to the *large-particle-only* distribution, *i.e.*, the PDF that is obtained by only considering the q values of the large-particle neighborhoods (the radical Voronoi diagram is *not* altered). This large-particle-only distribution is cut up into subdomains running from $q_r(i-1) < q \leq q_r(i)$ with $i = 4, 5, \text{etc.}$ On each of these subdomains, I establish the (sub)mode of the distribution — the value of ϕ for which the highest (local), large-particle-only PDF is found. Here, I specifically examined pentagonal and hexagonal neighborhoods, as these are most prevalent in the bidisperse disk system at high values of ϕ , also see Appendix B. The value of the PDF associated with this submode, denoted P_i^* , is shown in Fig. 5a-c as a function of ϕ for the two

domains $i = 5$ (blue; square to pentagon) and $i = 6$ (red; pentagon to hexagon), respectively.

Note that P_5^* has a clear minimum, see Fig. 5a-c. Taking the natural logarithm of P_5^* gave this minimum the appearance of a cusp. Both sides of this cusp were subsequently fitted using polynomials and the intersection point computed [91]. The associated value of ϕ , say ϕ^* , is shown in Fig. 5d, where the error bar gives an indication of the accuracy of the fit. The value of ϕ^* for $R > 0.83$ is indicated in magenta and for $R < 0.83$ in orange, respectively. I will return to the need for this distinction shortly. I also examined the distribution $P_\phi(q)$, which derives from *all* particle neighborhoods, and the PDF that results by considering only those neighborhoods that belong to *small* particles. In both distributions, the effect for the square-to-pentagon subdomain was clearly present for values of $R \uparrow 1$, but for $R \lesssim 0.83$ there were only small hints of a feature in the distribution, which proved difficult to fit, see the ESI [59]. This further justifies my choice for examining only the large particles.

Large particles, especially for $R \ll 1$, should be the least mobile and, thus, arrested dynamics should originate with these particles. This could explain why I see the strongest signal originating from this particle fraction. I find that the q associated with P_5^* shifts ever closer to $q_r(5)$ as ϕ is increased, with the peak-value first increasing, then decreasing rapidly, see the ESI for additional details [59]. In all cases, the decrease sets in as the large-particle neighborhoods tend toward hexagonal, *i.e.*, beyond the large-particle crossover $P_5^* = P_6^*$. This is when the large particles start to form hexagonal-like clusters to allow the system to further densify.

Note that whenever the system has a sufficiently large size asymmetry, the presence of the small particles interferes with the clustering and P_6^* reduces as ϕ is increased further. Following the vertical purple dashed lines, there is a strong correlation between this downward trend in P_6^* and the presence of the minimum in P_5^* (for sufficiently small R). However, the maximum in P_6^* proved more difficult to fit and I therefore did not do this. The intuition is that if the dynamics of the system drastically changes, one would expect there to be frustration. This will lead to local neighborhoods distorting, *e.g.*, see Ref. [54], rather than the system favoring neighborhoods that are close to $q_r(n)$. This can also be seen in Fig. 2a-c.

Examining the orange data in Fig. 5d, I note that the extracted value of ϕ^* lies somewhere between the curves $\max_\phi(n_{\bar{q}})$ and ϕ_a . Thus, within the limitations of my numerical analysis, I do not find a direct structural indicator of ‘arrested dynamics’, but one that is very close to it. I provide an additional analysis in Appendix E that is moderately successful in establishing the ϕ_a line. This suggests that slightly more extensive local measures of the structure, say also accounting for the next-nearest neighbors, would likely be able to locate ϕ_a more accurately.

Intriguingly, the minima in P_5^* are also present for $R \gtrsim 0.83$, as indicated by the magenta data in Fig. 5d. It appears that the mean value of ϕ^* on this domain

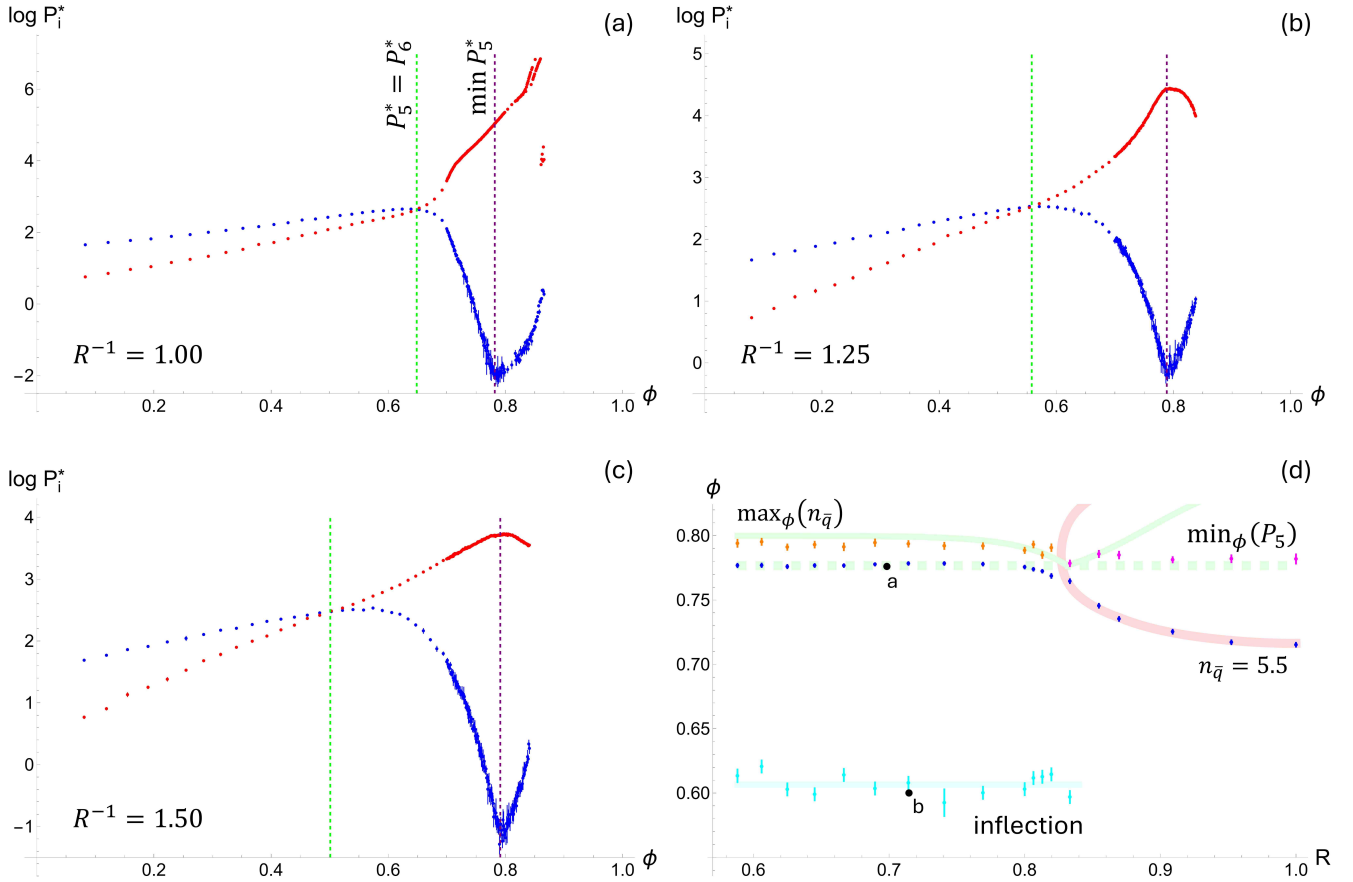


FIG. 5. **Identifying the arrested dynamics *via* the isoperimetric-quotient distribution.** (a-c) The (natural) logarithm of the isoperimetric-quotient PDF for *large* particles only, evaluated at its domain-restricted mode value P_i^* , as a function of the area fraction ϕ . The main text details the procedure by which this data was obtained. Blue points show the value for the submode restricted to the domain $q_r(4) < q \leq q_r(5)$ (P_5^*) and red points are obtained from data restricted to $q_r(5) < q \leq q_r(6)$ (P_6^*), respectively. The vertical dashed purple line indicates the local minimum, in this representation this is the location of the cusp in P_5^* , while the green one indicates the ϕ , for which the red and blue curves cross each other for the first time. In all cases, the value of the size ratio is labelled in the bottom-left corner of the panel. The error bars indicate the standard error of the mean, though in panel (a) there is a clear set of outliers. These were ignored in my analysis. (d) Reproduction of part of the R - ϕ state diagram of Fig. 4. The orange and magenta data shows ϕ associated with the minimum in the large-particle P_5^* and the cyan data indicates the inflection point in the diffusion data, see Section V. The black point labelled “a” corresponds to the glass transition found in Ref. [1]. The black point labelled “b” represents the “onset glass transition” as reported in Ref. [2]. All thick, light-colored curves serve as guides to the eye.

is slightly lower than that for smaller R (orange data). That is, ϕ^* lies closer to the green dashed line. This shows, to the best of my understanding for the first time, a structural indicator of the system changing within the crystalline phase. Though it should be noted that what I am picking up on is a very small effect. The same effect is present when only focusing on $P_{\phi}(q_r(5))$. Examination of system snapshots for $\phi \approx 0.777$ and $R \gtrsim 0.83$ does not reveal anything profound in the structure of the crystalline phase. That is, the particle arrangements appear to follow a standard hexagonal pattern, without obvious signs of defects or dislocations. This is, however, expected as the presence of pentagonal neighborhoods has dropped off to nearly zero, see Appendix B. The signal that P_5^* picks up is thus a signpost, the origin of which requires

interpretation, which I will provide in Section VIII.

B. Inflection Point for the Diffusivity

Figure 5d also shows the inflection point data (cyan) that was obtained from the measurement of the diffusion coefficient, see Section V. This could only be accurately established for $R \lesssim 0.83$, hence it is not shown over the entire range. There is a substantial error in the data, because it is a difficult point to extract. Note, however, that within this error, the associated value of ϕ is effectively constant. This is similar to the way ϕ_a behaves on this domain. Unlike for ϕ_a , I was unable to determine a structural feature that I could convincingly correlate to

the ϕ of the inflection point.

I suspect that this inflection point is set by the dynamics of the system changing from freely diffusing in a medium-dense environment to cage-like. The caging transition could not be readily obtained from the data that was available in Lozano *et al.* [1]. However, I note that Li *et al.* [2] studied a 55:45 (close to the 50:50 system) of small and large spheres (2.08 μm and 2.91 μm , respectively, resulting in $R \approx 0.72$) in quasi-2D confinement. I will thus rely on this data to make a comparison, see the black point labeled “b” in Fig. 5d, under the assumption that the small change in stoichiometry does not affect the system significantly.

The authors of Ref. [2] perturb their sample using a focused laser and track the particle displacement that this causes. They report a peak in the associated displacement values around $\phi \approx 0.6$, which I have used in my comparison. This peak is collocated with the *onset* of glassy dynamics according to the authors. However, despite the apparent similarities to the peak in Ref. [1] the origin seems different. That is, the MSD data in Ref. [2] does not reveal a clear glass transition; if such a transition is present, it may be that it occurs above $\phi > 0.73$. Thus, Li *et al.* interpret their point as being related to the formation of cages and therefore dub it an “onset glass transition.”

Despite the differences between Refs. [1] and [2], the indication seems that the signals picked up on by the respective approaches have to do with the dynamics of the local neighborhoods. The presence of a structural indicator appears more fortuitous than profound, but I will show that this is not the case next.

VIII. GEOMETRIC UNDERSTANDING

The above evidence points to the significance of the area fraction $\phi \approx 0.777$. In line with previous studies into this topic, the structural signifiers of (apparent) arrested dynamics are relatively weak [53, 54]. My shell-percolation approach in Appendix D tracks ϕ_a very accurately. However, it relies on a large amount of data to obtain a result of this quality, as well as on comparison between closely spaced values of ϕ to arrive at an appropriate match to ϕ_a . Similarly, the identification which is based on the cusp in $\max_\phi(n_{\bar{q}})$, see Section VI, and the cusp in the large-particle-only abundance of pentagonal neighborhoods, see Section VII A, require large data sets to identify a small, but real effect. I also considered a form of Voronoi entropy [92] based on the isoperimetric quotient, which showed a weak signal near ϕ_a ; it was therefore not reported on here.

Nonetheless, a structural effect is present and I will thus explore this aspect further. The ‘ideal’ or ‘pure’ structural signal, I must conclude, is somehow obscured. To uncover it, I turn to a granocentric-inspired [93–95] view of the particles. This choice is also informed by the fact that I make a tentative connection to random loose

packing in Appendix A. That is, the granocentric approach has been applied to study random packings. The results in Section VII A show that it is sensible to focus on $R = 1$, as there are features of this system that are shared by those with $R \lesssim 0.8$ that do not crystallize. I will now argue how using a granocentric approach leads to a structure-based transition at $\phi_g = \sqrt{3}\pi/7 \approx 0.777343$.

A. Introducing the Floret Pentagonal Tiling

It is straightforward to show that a small particle can be stabilized by being surrounded by 5 larger particles, leading to a pentagonal neighborhood. At contact, this occurs for $R \approx 0.701302$; the ESI [59] provides the analytic expression. Large particles can have a perfectly heptagonal neighborhood, whenever they are surrounded by 7 small particles. At contact, this occurs for $R \approx 0.766422$, also see the ESI [59]. Neither of these values corresponds particularly well with the transitions observed in the system. It should be clear that the presence of such neighborhoods is a rarity. Thus, I would not expect the appearance of arrest to be captured by such a simple picture. Interference with crystallization should ideally be shared equally among all particles.

Figure 6a shows a single, pentagonal neighborhood of a central disk surrounded by five neighbors, which meets this requirement. It is easy to demonstrate, see the ESI [59], that the volume fraction associated with this central particle is $\phi = \sqrt{3}\pi/7$. These neighborhoods can be assembled into a regular structure that is effectively a close-packed hexagonal crystal with one particle out of every 7 missing, see Fig. 6b. For each collection of 6 particles surrounding a void, henceforth referred to as ‘wheel’, every particle is in contact with 5 neighbors. Thus, every associated Voronoi cell has exactly 5 vertices. This also means that the particle is completely immobilized, independent of whether it is frictional or non-frictional.

The structure in Fig. 6b is known from the field of pentagonal tilings, *i.e.*, it is a monohedral, convex, pentagonal tiling of type 6 [72, 73]. It is also often referred to as a floret pentagonal tiling (FPT). I will refer to the particle stacking into ordered wheels as an FPT structure in recognition of this connection. For my intents and purposes, however, it is important that the tiling follows from a Voronoi tessellation argument that respects the size of the particles and has congruent tiles.

Note that the Voronoi vertex in the center of each wheel is 4-fold degenerate. That is, if one were to consider a wheel in isolation and perturb the particle positions from their contact, one would be able to gain 3 additional vertices by some of the particles becoming neighbors. This could be done, *e.g.*, by reducing the overall area fraction, which would give each particle freedom to move. In practice, there are thus 6 Voronoi-cell edges per particle on average in the FPT structure. This is likely why it is so difficult to pick up on FPT Voronoi-cell signals in the thermalized systems.

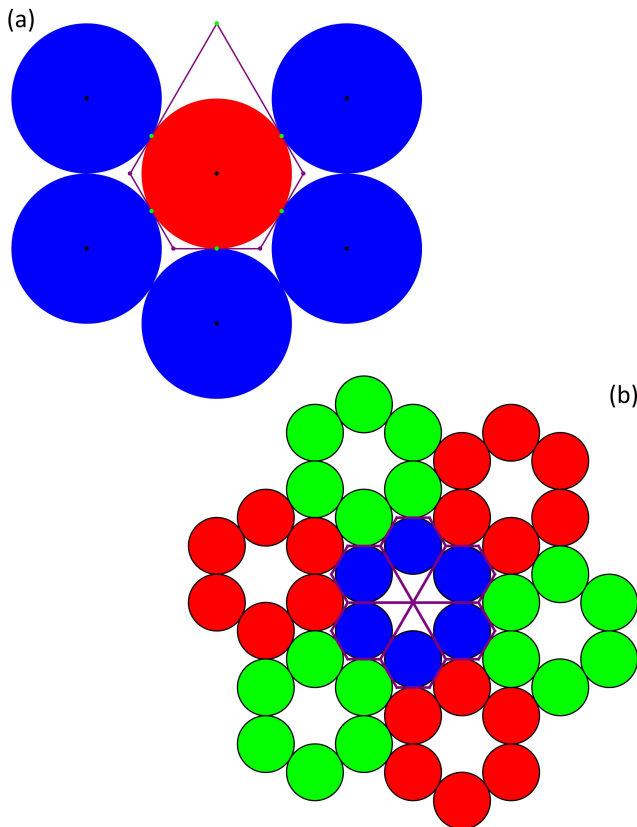


FIG. 6. **Geometric ground state that can be related to the glass transition.** (a) The Voronoi cage (purple) around a single particle (red) surrounded by 5 neighboring disks (blue). These particles are in contact (green points). The black dots indicate the centers of the respective disks. (b) Organizing the particles into ‘wheel’-like neighborhoods, wherein all the Voronoi cells have five vertices. The central wheel (blue) shows the 6 pentagonal Voronoi cells (purple). The six surrounding wheels show that these can be stacked into a crystalline structure. The use of alternating red and green coloring is meant to help distinguish the wheels, but otherwise carries no physical significance.

B. A Geometric Ground State

It is clear that the structure in Fig. 6b is a crystalline solid and mechanically rigid. In particular, it cannot be melted into a fluid at a constant ϕ . In fact, one can remove particles from each wheel, without impairing the rigidity, as each particle in the system has 5 contact points. At most two particles per wheel can be removed, for a structure that is still ordered at a longer range and maintains rigidity. This does come at the cost of having two types of Voronoi cell, which I consider undesirable, as will become clear in Section VIII E. The FPT has a single realization and this means its configurational entropy is zero. Removing or adding particles moves ϕ (slightly) away from $\sqrt{3}\pi/7$ in either direction. However, it simultaneously strongly increases the configurational entropy. For a monodisperse hard-disk system, I will refer to the

FPT as a ‘geometric ground state’ at $\phi = \phi_g$, *i.e.*, it is the lowest entropy configuration in the ($T \downarrow 0$) limit.

Now we can turn to bidisperse (possibly also polydisperse) systems. In the thermodynamic limit ($N \uparrow \infty$), one can easily discount edge effects and place all particles of the same size in their own FPT. That is, one would have several contacting areas of specific size particles in FTP with mismatching lattice size. Thus, provided features of the structure in Fig. 6b are responsible for the appearance of ϕ_a , the associated ϕ should be (relatively) independent of R . This agrees with my findings for $R \lesssim 0.8$ in Section VI, and would also explain the appearance of some structural features at $\phi \approx 0.777$ for $R \gtrsim 0.8$. Any variations that were observed on these are likely due to finite-size effects or other physical mechanisms interfering, such as proximity to the ‘critical point’ in $n_{\bar{q}} = 5.5$. Turning to Appendix A, it then also becomes clear why point ‘g’ in Fig. 8, which was obtained for another stoichiometric ratio (1:2) [96], is close to ϕ_g . In principle, if there is only a geometric requirement, then it is likely that signatures of ϕ_g can be recovered in polydisperse systems, provided there is sufficient statistics.

C. Glass, Frustrated Disorder, or Something Else

Systems with $R \approx 1$ tend to crystallize into a hexagonal configuration, rather than an FPT structure. This is well-known from the literature [96] and makes sense. That is, intuitively the disks can make their density homogeneous by locally arranging into a hexagonal crystal rather than an FPT. Thermodynamically, the state in Fig. 6b is also unfavored for $T > 0$, because there is only a single realization, for which all Voronoi cells are identical and pentagonal. When assuming a hexagonal crystal configuration at $\phi = \phi_g$, the particles can vibrate about their ideal hexagonal-lattice position, raising both the configurational and vibrational entropy of the system.

The shape of the red curve in Fig. 4 suggests that the role of R is akin to that of temperature in a regular phase diagram. This led me to adopt the wording ‘critical point,’ when referencing the left-most point of the red curve in the state diagram, see Section VI. Given that ϕ_a is extracted from the limiting behavior of the diffusion coefficient $D(\phi) \downarrow 0$, it is sensible to assume that this is not a critical point in the equilibrium sense of the word. Note, however, that while the long-time linear part to the MSD is quickly dropping off, there is displacement at sufficiently long times. Thus, to state definitively that the system has fallen out of equilibrium is not accurate.

This is also evidenced by the SISF data in the experiment of Lozano *et al.* [1], which only shows a divergent relaxation time near rcp. I therefore conclude that there is *no* glassy dynamics at their measured $\phi \approx 0.776$ and that the (nearly) constant feature at $\phi \approx 0.777$ in my simulations is present in equilibrium. I used the time-dependent data to gain additional insight by analyzing the way neighborhoods change, see the ESI [59].

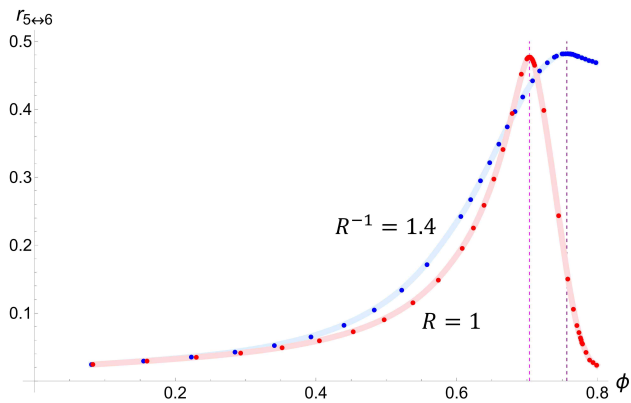


FIG. 7. **The relative neighborhood exchange rate indicates strong fluctuations close to transitions.** The ratio of the number of changes between a pentagonal and a hexagonal neighborhood to the total number of particle displacements in the system, $r_{5\leftrightarrow 6}$, as a function of the area fraction ϕ . The red and blue points show data gathered for $R = 1$ and $R^{-1} = 1.4$, respectively, as labelled. The solid, light-red and light-blue curves serve to guide the eye. The peak positions are indicated by the magenta and purple vertical dashed lines, respectively. Errors are smaller than the symbol size and therefore not shown here.

In brief, for each time step, I compute the radical Voronoi diagram and keep track of the q value belonging to each particle. I find that for sufficiently high ϕ , the neighborhoods dwell about integer values of n_q and the system does not favor half-integer n_q . For example, the trajectory of a certain particle may lead it to explore pentagonal ($n_q \approx 5$) and hexagonal ($n_q \approx 6$) neighborhoods, but spend little time in 5.5-gonal neighborhoods [97]. Next, I extract transition rates for the exchange between neighborhoods and normalized this by the total number of particle displacements in the system. This resulted in, for example, relative exchange rates between pentagonal and hexagonal neighborhoods, $r_{5\leftrightarrow 6}$, some which are shown in Fig. 7.

Surprisingly, the relative number of exchanges constitutes a substantial fraction of particle displacements even at high ϕ close to ϕ_a or equivalently ϕ_g . This means that while there is relatively limited cage hopping, as evidenced by the low value of $D(\phi)$, the cages themselves are quite dynamic. Additionally, I find no significant difference in the $r_{i\leftrightarrow i+1}$ between small and large particles for any integer i , see the ESI [59]. This implies that the cage dynamics is shared equally among the large and small particles, though it does not exclude a difference in cage-hopping rate, *i.e.*, in diffusivity.

Both data sets presented in Fig. 7 show a peak. When there is crystallization, as is the case for $R = 1$, it is sharp and very pronounced. Fitting the peak values results in $\phi \approx 0.703$ and $\phi \approx 0.757$ for $R = 1$ and $R^{-1} = 1.4$, respectively. The former agrees very well with where the fluid state is expected to become unstable. The latter is close to, but not quite at ϕ_g . For $R^{-1} = 1.4$, the

peak is also broader and less pronounced. Within the error, I detected no discernable drift toward one type of neighborhood as a function of time. This suggests that there is *no* slow relaxation toward a phase-separated state, as would be the case for glassy dynamics.

That the rate of cage rearrangement is relatively high, fits with the conceptual picture of an active probe particle (experiments in Ref. [1, 61]) picking up on the fluctuations of the local environment, as put forward in recent modeling work from my group [60, 61]. The fact that $r_{5\leftrightarrow 6}$ is asymmetric about $\phi \approx \phi_g$ would also fit with the asymmetric probe response observed in Ref. [1]. However, there is a slight mismatch between the peak value of ϕ and ϕ_g . This should be addressed in future work, wherein active probes are included in the sample, but this falls outside of the scope of the present research.

Weighting the evidence, I believe that the frustration experienced by the system at $\phi = \phi_g$ can be attributed to the special properties of the FTP lattice, rather than kinetic arrest. That being said, the geometric ground state may be a deep (local) entropic minimum for $T = 0$, but at finite temperature, it is not obvious why the FPT should be important. In fact, it is extremely likely that FTP cannot form for $T > 0$. I will address how to reconcile these two seemingly conflicting points in Section VIII E.

D. Other Geometric Ground States

Before getting to that, let us consider if there is additional evidence that could support my viewpoint by examining other geometric-ground-state candidates. An equilateral-triangle tessellation of Voronoi cells forms when the particles are placed in contact in a regular honeycomb lattice. Each particle then has 3 neighbors, which makes the structure mechanically unstable, unless the particles are fully frictional. The close-packing honeycomb lattice gives an area fraction $\phi_t = \pi/(3\sqrt{3}) \approx 0.605$. This is the lowest density lattice, for which the particles can be made to touch in such a way that equal-shape triangular Voronoi cells are obtained.

Note that ϕ_t is close to where I observe an inflection point in the derivative of the diffusion coefficient, see Section V. In fact, the guide to the eye in Fig. 5d is a fitted constant with value $\phi \approx 0.607$ to all the data points, which matches the ϕ_t value very well. In addition, the predicted honeycomb-lattice ϕ is close to where Li *et al.* [2] locate their “onset glass transition” / the appearance of caging in the fluid. Adopting the geometric-ground-state viewpoint, it makes sense that for the $\phi = \phi_t$, the response of the fluid to external perturbations is strongest.

Turning to regular, square Voronoi cells, I find that they form by a simple-square stacking of disks with $\phi = \pi/4$. This structure is isostatic, but not stable to shear deformation for frictionless disks. The ϕ value lies close to, but measurably above, where I report ϕ_a in the system. There are several potential signals of a square-

only ground state. Firstly, the area fraction associated with the ‘critical point’ in $n_{\bar{q}} = 5.5$ curve: $\phi \approx 0.785$ for $R^{-1} \approx 1.21$. This value matches closely $\phi = \pi/4$, although I acknowledge there is substantial uncertainty to determining this point. Potentially, the P_5^* -minimum data in Fig. 5d can also be ascribed to the presence of a square-tiling ground state. However, the mean value of this data appears to lie at a slightly higher value of $\phi \approx 0.793$. This is both within two standard deviations ($\sigma_\phi \approx 0.005$) of the $\phi = \pi/4$ and the $\max_\phi(n_{\bar{q}})$ line. It is therefore difficult to draw any substantial conclusions about the effect of a potential square-tiling geometric ground state. Presumably this is also because $\phi_g < \pi/4$ and associated with a much more stable FTP tiling.

E. Connection to Foam-like Tissue Models

I had set out to make the connection to the literature on foam-like tissue modelling [62–69]. Taking on this viewpoint, one can see the presence of the FPT ground state at $\phi = \phi_g$ as the particle equivalent to imposing a shape index belonging to a regular pentagon for epithelia/foam models. If this is a correct viewpoint, a geometric or topological reasoning may be given for the appearance of the structural and dynamic features at $\phi = \phi_g$.

The first thing to note is that the connection is not simple. The value of q associated with the FTP lattice is $q \approx 0.777$, which is close to $q_t(4) = \pi/4 \approx 0.785$. In a foam-like model with a Hamiltonian of the form in Eq. (1), the equivalent shape index would place the system firmly in the fluid-like state. To observe jamming in such a system requires $q \approx 0.865$ (value for a regular pentagon) [62]. This suggests that a direct mapping to foam-like models with Eq. (1) is not possible.

Nonetheless, there are several aspects that suggest there is a path forward. Examining the single-particle neighborhood in my granocentric analysis, I found that the isoperimetric quotient q is identical to the associated (local) volume fraction ϕ_g . This seems to be a robust result for a range of neighborhood configurations involving particles that are in contact, see the ESI [59]. Contact-preserving distortions may therefore leave \bar{q} unaffected. Note, however, that this constancy does not hold when the particles are out of contact. That is, the observed mean value of q is not the same as the FTP one. In the range where ϕ_a is nearly constant, I measure $\bar{q} \approx 0.88$. This need not immediately discount the intuition about the geometric ground state. For the foam-like tissue models, the mean shape index is also not necessarily equal to the one that is imposed.

Nonetheless, it is well known that certain topological properties are invariant under diffeomorphism, as are other invariants [98]. I have already stated that the FTP structure cannot be broken up to form a fluid (there are 5 neighbors per particle), nor can it be formed from a fluid phase in a defect-free manner. However, consider a FTP structure which has two adjacent vacancies in one of its

wheels, but is otherwise perfect. Then it is clear that the structure may be systematically ‘stripped’ from this central point out into a crystalline structure, which may subsequently be made (to appear) disordered. Thus it seems likely that a diffeomorphism, barring an intensive subset of the FTP lattice, can be constructed.

At present, a full mathematical framework by which the connection can be proven, appears out of reach. Other candidates for making the connection involve the study of cage transformations and T1-transitions [62, 99–104]. It may also be possible to repurpose the quasi-species approach of Ref. [105], as I suspect the behavior that I find is *in equilibrium*. However, for now, such an effort must be left to future work.

IX. DISCUSSION

Thus far, I have avoided speaking of the ‘ideal glass transition’. That is, the presence of a disordered system of particles with zero configurational entropy. This has been a topic of significant interest [96, 106, 107], with a very recent study focusing on 2D [108]. Given the requirements for a glass transition, the constant ϕ_a range *cannot* be identified as such, as I observed earlier in Section VIII C. Nonetheless, there is compelling evidence for a structural transition that underlies my observations. This transition I would identify as a continuous one, given the smoothness of the $R \lesssim 0.83$ curves in Appendix D.

I would further like to note that the concept of a geometric reference is by no means a new one. However, it is typically applied locally, for example, when examining the dynamics in glasses [2, 9, 22, 23, 42, 49, 109]. What has not been previously reported, to the best of my understanding, is that seemingly disordered (2D hard-disk) particle fluids can become entangled with geometric, regularly ordered ground states. Given the recent successes of machine learning techniques in determining the dynamic propensity of particles [36, 37, 40], it seems likely that the application of such a machine-learning approach would be able to pick up on ϕ_a .

Thus far, I have spoken about geometry, which makes sense for hard-particle systems. In systems where the particles interact *via* soft potentials, it is not obvious whether the argument can be made by solely by considering the particle arrangement. However, I would expect that elements of the geometric ground state are preserved in such soft systems. I base this intuition on fact that foam-like tissue models [62–69] have Harmonic potentials governing their dynamics, yet show jamming due to geometric frustration.

I alluded to the potential for random-loose packing (rlp) to be associated with the appearance of glassy dynamics in my comparison to the literature in Appendix A. Reflecting on this, I would think that this relation is tenuous at best. The FTP has 5 neighbor contacts, which is well above the isostatic requirement of 3 (frictional) or 4 (frictionless) contacts. I suspect that the origin of

the observation in Ref. [110] may be attributed to the intervention of the transition that I have picked up in the data. That is, the presence of the FTP geometric ground state might have biased the simulation toward placing rlp close to ϕ_g . The rlp connection in the numerical work of Refs. [111, 112] could be similar in nature. However, the connection is also found in 3D systems.

It is possible that the notion of a geometric ground state can be transferred to 3D systems. In Appendix F, I analyze several candidate structures. In foam-like tissue modeling, there is evidence that a geometric frustration similar to the one in 2D can occur [113]. In addition, when the particles are arranged using the underlying structure of a (non-gyrate) tetrahedral-octahedral honeycomb, I obtain a volume fraction of $\eta = 8\pi/(27\sqrt{3}) \approx 0.537422$. In this arrangement, the particles are the inscribed spheres to the octahedra comprising the honeycomb. This packing fraction is relatively close to the reported rlp value for frictional spheres in 3D, $\eta \approx 0.536$ [44], though it is often placed at a slightly higher value of $\eta \approx 0.555$ in experimental studies [114]. However, it should also be clear that 3D systems are quite different from their 2D counterparts. The exploration of 3D is therefore left to follow-up work.

Lastly, I should address potential for experimental validation. Local rheological characterization using active particles [1] and perturbing the system via local laser illumination [2], both have the potential to reveal structural and dynamical changes. It would be useful to see to what extent either approach reveals the presence of near-constant ϕ features in the $R - \phi$ state diagram, as predicted by the simulations performed here. It would additionally be useful to identify the presence of the underlying FTP structure directly. However, at present it is less clear how to approach this without gathering considerable statistics, as was done here. Future work will focus on developing the theory behind the connection and this effort may reveal a more direct quantifier.

X. CLOSING REMARKS

Summarizing, in this paper, I have shown a clear relation between geometry and dynamic features in two-dimensional bidisperse systems of hard disks. This was underpinned by careful analysis of the isoperimetric quotient and mean squared displacement. Surprisingly, the system appears to fall out of equilibrium for a nearly constant value of the area fraction $\phi \approx 0.777$ over a wide range of disk size ratios $R \lesssim 0.83$. I link this feature in the state diagram to the existence of a geometric ground

state. Therein the disks are in contact and arranged in such a manner that their Voronoi cells form a floret pentagonal tiling of the plane. This configuration has an area fraction of $\phi_g = \sqrt{3}\pi/7 \approx 0.777343$, which is in excellent agreement with the observed value of $\phi \approx 0.777$.

I have argued that the existence of such a regular, geometric ground state echoes through in the disordered, finite-temperature system, causing its dynamics to change drastically. This is similar to the way in which the shape index can influence the dynamics in a foam-like tissue models. In terms of the dynamics, the transition picked up in earlier experiments by Lozano *et al.* [1], has features that are reminiscent of glassy dynamics. However, based on the data presented here, it should not be identified as such. Instead, the viewpoint that I present in this paper, strongly suggests that one should see dense 2D fluids as something else than disordered systems. They may be entangled with ordered, zero-entropy ground states that can enforce geometric frustration even at finite temperature. This perspective could also help explain the observations by Li *et al.* [2].

Future work in this direction should focus on making the suggested connection mathematically rigorous. I have already briefly discussed extensions to 3D and soft systems in this paper, which provide routes for further exploration of the topic. While presently it appears that the transition obtained in the 2D bidisperse disk systems is not a glass transition, it may also be interesting to see how the concepts introduced here can be modified to help understand structural glass formers.

XI. ACKNOWLEDGEMENTS

The author acknowledges financial support from the Netherlands Organization for Scientific Research (NWO) through Start-Up Grant 740.018.013. I am grateful to Frank Smalenburg for making his code available for use [71], which proved instrumental in the realization of this project, as well as for useful discussions on the analysis. I further acknowledge Edan Lerner for a critical reading of a draft version of the manuscript, which helped me substantially refine my perspective, and Celia Lozano for providing the raw self-intermediate scattering data [1]. Lastly, I would like to thank Luca Giomi, Clemens Bechinger, Roel Dullens, and Alptug Ulugöl for providing useful input on my work.

An open-data package containing the means to reproduce the figures and overall results of the simulations is available at: [\[url to be inserted\]](#).

[1] C. Lozano, J. Gomez-Solano, and C. Bechinger, Active particles sense micromechanical properties of glasses, *Nat. Mater.* **18**, 1118 (2019).

[2] B. Li, K. Lou, W. Kob, and S. Granick, Anatomy of cage formation in a two-dimensional glass-forming liquid, *Nature* **587**, 225 (2020).

- [3] H. Sillescu, Heterogeneity at the glass transition: a review, *J. Non-Cryst. Solids* **243**, 81 (1999).
- [4] L. Berthier, G. Biroli, J.-P. Bouchaud, L. Cipelletti, and W. van Saarloos, *Dynamical heterogeneities in glasses, colloids, and granular media*, Vol. 150 (OUP Oxford, Oxford (United Kingdom), 2011).
- [5] G. Hunter and E. Weeks, The physics of the colloidal glass transition, *Rep. Prog. Phys.* **75**, 066501 (2012).
- [6] S. Karmakar, C. Dasgupta, and S. Sastry, Length scales in glass-forming liquids and related systems: a review, *Rep. Prog. Phys.* **79**, 016601 (2015).
- [7] V. Manoharan, Colloidal matter: Packing, geometry, and entropy, *Science* **349**, 1253751 (2015).
- [8] E. Weeks, Introduction to the Colloidal Glass Transition, *ACS Macro Lett.* **6**, 27 (2017).
- [9] H. Tanaka, H. Tong, R. Shi, and . Russo, Revealing key structural features hidden in liquids and glasses, *Nature Reviews Physics* **1**, 333 (2019).
- [10] H. Lindsay and P. Chaikin, Elastic properties of colloidal crystals and glasses, *J. Chem. Phys.* **76**, 3774 (1982).
- [11] P. Pusey and W. van Meegen, Phase behaviour of concentrated suspensions of nearly hard colloidal spheres, *Nature* **320**, 340 (1986).
- [12] P. Pusey and W. van Meegen, Observation of a glass transition in suspensions of spherical colloidal particles, *Phys. Rev. Lett.* **59**, 2083 (1987).
- [13] Here, I am purposefully circumspect in using the word ‘transition’, since the formation of a glass is unlike well-known transitions such as freezing or melting. The latter two involve discontinuities in derivatives of the free energy and are therefore readily identified as true transitions. The formation of a glass, however, appears to follow a smooth increase in the viscosity of dozens (if not more) orders of magnitude. This also means that the system typically falls out of equilibrium and the free energy cannot be properly defined.
- [14] The more commonly referenced quantity of temperature, *i.e.*, glass-transition temperature, is not particularly relevant for hard-sphere systems, as it merely scales the unit of time.
- [15] K. Binder and W. Kob, *Glassy materials and disordered solids: An introduction to their statistical mechanics* (World scientific, Singapore (Singapore), 2011).
- [16] G. Brambilla, D. El Masri, M. Pierno, L. Berthier, . Cipelletti, G. Petekidis, and A. Schofield, Probing the Equilibrium Dynamics of Colloidal Hard Spheres above the Mode-Coupling Glass Transition, *Phys. Rev. Lett.* **102**, 085703 (2009).
- [17] S. Vivek, C. Kelleher, P. Chaikin, and E. Weeks, Long-wavelength fluctuations and the glass transition in two dimensions and three dimensions, *Proc. Natl. Acad. Sci.* **114**, 1850 (2017).
- [18] J. Hallett, F. Turci, and C. Royall, Local structure in deeply supercooled liquids exhibits growing length-scales and dynamical correlations, *Nat. Commun.* **9**, 3272 (2018).
- [19] A. Liu, H. Pham, A. Bera, T. Petersen, T. Sirk, S. Mudie, R. Tabor, J. Nunez-Iglesias, A. Zaccone, and M. Baggioni, Measurable geometric indicators of local plasticity in glasses, *arXiv* **2410.09391**, 1 (2024).
- [20] S. Schoenholz, E. Cubuk, D. Sussman, E. Kaxiras, and A. Liu, A structural approach to relaxation in glassy liquids, *Nat. Phys.* **12**, 469 (2016).
- [21] A. Ninarello, L. Berthier, and D. Coslovich, Models and algorithms for the next generation of glass transition studies, *Phys. Rev. X* **7**, 021039 (2017).
- [22] H. Tong and H. Tanaka, Revealing hidden structural order controlling both fast and slow glassy dynamics in supercooled liquids, *Phys. Rev. X* **8**, 011041 (2018).
- [23] S. Marín-Aguilar, H. Wensink, G. Foffi, and F. Smallenburg, Tetrahedrality dictates dynamics in hard sphere mixtures, *Phys. Rev. Lett.* **124**, 208005 (2020).
- [24] L. Berthier and D. Reichman, Modern computational studies of the glass transition, *Nature Rev. Phys.* **5**, 102 (2023).
- [25] A. Bera, M. Baggioni, T. Petersen, T. Sirk, A. Liu, and A. Zaccone, Clustering of negative topological charges precedes plastic failure in 3D glasses, *PNAS Nexus* **2024**, pga315 (2024).
- [26] G. Parisi and F. Zamponi, Mean-field theory of hard sphere glasses and jamming, *Rev. Mod. Phys.* **82**, 789 (2010).
- [27] L. Berthier and G. Biroli, Theoretical perspective on the glass transition and amorphous materials, *Rev. Mod. Phys.* **83**, 587 (2011).
- [28] L. Janssen, Mode-coupling theory of the glass transition: A primer, *Front. Phys.* **6**, 97 (2018).
- [29] C. Royall and S. Williams, The role of local structure in dynamical arrest, *Phys. Rep.* **560**, 1 (2015).
- [30] C. Xia, J. Li, Y. Cao, B. Kou, X. Xiao, K. Fezzaa, T. Xiao, and Y. Wang, The structural origin of the hard-sphere glass transition in granular packing, *Nat. Commun.* **6**, 8409 (2015).
- [31] E. Boattini, S. Marín-Aguilar, S. and Mitra, G. Foffi, F. Smallenburg, and L. Filion, Autonomously revealing hidden local structures in supercooled liquids, *Nat. Commun.* **11**, 5479 (2020).
- [32] E. Cubuk, S. Schoenholz, J. Rieser, B. Malone, J. Rottler, D. Durian, E. Kaxiras, and A. Liu, Identifying structural flow defects in disordered solids using machine-learning methods, *Phys. Rev. Lett.* **114**, 108001 (2015).
- [33] J. Paret, R. Jack, and D. Coslovich, Assessing the structural heterogeneity of supercooled liquids through community inference, *J. Chem. Phys.* **152**, 144502 (2020).
- [34] V. Bapst, T. Keck, A. Grabska-Barwińska, C. Donner, E. Cubuk, S. Schoenholz, A. Obika, A. Nelson, T. Back, and D. Hassabis, Unveiling the predictive power of static structure in glassy systems, *Nat. Phys.* **16**, 448 (2020).
- [35] D. Richard, M. Ozawa, S. Patinet, E. Stanifer, B. Shang, S. Ridout, B. Xu, G. Zhang, P. Morse, and J.-L. Barrat, Predicting plasticity in disordered solids from structural indicators, *Phys. Rev. Mater.* **4**, 113609 (2020).
- [36] R. Alkemade, E. Boattini, L. Filion, and F. Smallenburg, Comparing machine learning techniques for predicting glassy dynamics, *J. Chem. Phys.* **156**, 204503 (2022).
- [37] R. Alkemade, F. Smallenburg, and L. Filion, Improving the prediction of glassy dynamics by pinpointing the local cage, *J. Chem. Phys.* **158** (2023).
- [38] N. Oyama, S. Koyama, and T. Kawasaki, What do deep neural networks find in disordered structures of glasses?, *Front. Phys.* **10**, 1007861 (2023).
- [39] G. Jung, G. Biroli, and L. Berthier, Predicting dynamic heterogeneity in glass-forming liquids by physics-inspired machine learning, *Phys. Rev. Lett.* **130**, 238202 (2023).

- (2023).
- [40] G. Jung, R. Alkemade, V. Bapst, D. Coslovich, L. Filion, F. Landes, A. Liu, F. Pezzicoli, H. Shiba, G. Volpe, F. Zamponi, L. Berthier, and G. Biroli, Roadmap on machine learning glassy liquids, arXiv **2311.14752**, 1 (2023).
- [41] R. Sahu, M. Sharma, P. Schall, S. M. Bhattacharyya, and V. Chikkadi, Structural origin of relaxation in dense colloidal suspensions, Proc. Natl. Acad. Sci. **121**, e2405515121 (2024).
- [42] A. Sharma, C. Liu, and M. Ozawa, Selecting Relevant Structural Features for Glassy Dynamics by Information Imbalance, arXiv **2408.12705**, 1 (2024).
- [43] G. Hocky, D. Coslovich, A. Ikeda, and D. Reichman, Correlation of local order with particle mobility in supercooled liquids is highly system dependent, Phys. Rev. Lett. **113**, 157801 (2014).
- [44] C. Song, P. Wang, and H. Makse, A phase diagram for jammed matter, Nature **453**, 629 (2008).
- [45] S.-C. Zhao, S. Sidle, H. Swinney, and M. Schröter, Correlation between Voronoi volumes in disc packings, Europhys. Lett. **97**, 34004 (2012).
- [46] P. Morse and E. Corwin, Geometric signatures of jamming in the mechanical vacuum, Phys. Rev. Lett. **112**, 115701 (2014).
- [47] E. Bormashenko, M. Frenkel, A. Vilks, I. Legchenkova, A. Fedorets, N. Aktaev, L. Dombrovsky, and M. Nosonovsky, Characterization of self-assembled 2D patterns with Voronoi Entropy, Entropy **20**, 956 (2018).
- [48] W. Jin, A. Datye, U. Schwarz, M. Shattuck, and C. O’Hern, Using delaunay triangularization to characterize non-affine displacement fields during athermal, quasistatic deformation of amorphous solids, Soft Matter **17**, 8612 (2021).
- [49] S. Kim and S. Hilgenfeldt, Structural measures as guides to ultrastable states in overjammed packings, Phys. Rev. Lett. **129**, 168001 (2022).
- [50] P. Morse and E. Corwin, Local stability of spheres via the convex hull and the radical Voronoi diagram, Phys. Rev. E **108**, 064901 (2023).
- [51] V. Worlitzer, G. Ariel, and E. Lazar, Pair correlation function based on Voronoi topology, Phys. Rev. E **108**, 064115 (2023).
- [52] X. Du and E. Weeks, Rearrangements during slow compression of a jammed two-dimensional emulsion, Phys. Rev. E **109**, 034605 (2024).
- [53] H. Zhang, Q. Zhang, F. Liu, and Y. Han, Anisotropic-isotropic transition of cages at the glass transition, Phys. Rev. Lett. **132**, 078201 (2024).
- [54] J. Rieser, C. Goodrich, A. Liu, and D. Durian, Divergence of Voronoi cell anisotropy vector: a threshold-free characterization of local structure in amorphous materials, Phys. Rev. Lett. **116**, 088001 (2016).
- [55] G. Schröder-Turk, W. Mickel, M. Schröter, G. Delaney, M. Saadatfar, T. Senden, K. Mecke, and T. Aste, Disordered spherical bead packs are anisotropic, Europhys. Lett. **90**, 34001 (2010).
- [56] S. Kapfer, W. Mickel, K. Mecke, and G. Schröder-Turk, Jammed spheres: Minkowski tensors reveal onset of local crystallinity, Phys. Rev. E. **85**, 030301 (2012).
- [57] W. Mickel, S. Kapfer, G. Schröder-Turk, and K. Mecke, Shortcomings of the bond orientational order parameters for the analysis of disordered particulate matter, J. Chem. Phys. **138**, 044501 (2013).
- [58] L. Garca-Coln, L. Del Castillo, and P. Goldstein, Theoretical basis for the Vogel-Fulcher-Tammann equation, Phys. Rev. B **40**, 7040 (1989).
- [59] J. de Graaf, Electronic Supplemental Information, online (2024), database containing the source codes (C/C++) used to generate our results, as well as the analysis scripts (Mathematica and Python) used to obtain the results in the paper. The material used to create the figures (Mathematica/Powerpoint) in the main text and appendices is also provided. Every element is commented and additional analyses, referred to in the main text are also provided.
- [60] C. Abaurrea-Velasco, C. Lozano, C. Bechinger, and J. de Graaf, Autonomously probing viscoelasticity in disordered suspensions, Phys. Rev. Lett. **125**, 258002 (2020).
- [61] N. Narinder, M. Bos, C. Abaurrea-Velasco, J. de Graaf, and C. Bechinger, Understanding enhanced rotational dynamics of active probes in rod suspensions, Soft Matter **18**, 6246 (2022).
- [62] D. Bi, J. Lopez, J. Schwarz, and M. Manning, A density-independent rigidity transition in biological tissues, Nat. Phys. **11**, 1074 (2015).
- [63] D. Bi, X. Yang, M. Marchetti, and M. Manning, Motility-driven glass and jamming transitions in biological tissues, Phys. Rev. X **6**, 021011 (2016).
- [64] D. Barton, S. Henkes, C. Weijer, and R. Sknepnek, Active vertex model for cell-resolution description of epithelial tissue mechanics, PLoS Comput. Biol. **13**, e1005569 (2017).
- [65] X. Yang, D. Bi, M. Czajkowski, M. Merkel, M. Manning, and M. Marchetti, Correlating cell shape and cellular stress in motile confluent tissues, Proc. Natl. Acad. Sci. **114**, 12663 (2017).
- [66] L. Atia, D. Bi, Y. Sharma, J. Mitchel, B. Gweon, S. Koehler, S. DeCamp, B. Lan, J. Kim, and R. Hirsch, Geometric constraints during epithelial jamming, Nat. Phys. **14**, 613 (2018).
- [67] L. Yan and D. Bi, Multicellular rosettes drive fluid-solid transition in epithelial tissues, Phys. Rev. X **9**, 011029 (2019).
- [68] M. Krajnc, Solid–fluid transition and cell sorting in epithelia with junctional tension fluctuations, Soft Matter **16**, 3209 (2020).
- [69] O. Damavandi, E. Lawson-Keister, and M. Manning, Universal features of rigidity transitions in vertex models for biological tissues, bioRxiv **494406**, 2022 (2022).
- [70] Technically, this only holds for vertex models in the zero-temperature limit [115].
- [71] F. Smallenburg, Efficient event-driven simulations of hard spheres, Eur. Phys. J. E **45**, 22 (2022).
- [72] D. Schattschneider, Tiling the plane with congruent pentagons, Math. Mag. **51**, 29 (1978).
- [73] C. Alsina and R. Nelsen, *A panoply of polygons*, Vol. 58 (American Mathematical Society, Providence, USA, 2023).
- [74] I performed a small number of simulations with 10,000 particles, which showed little difference to the results obtained for a smaller number of particles.
- [75] K. Desmond and E. Weeks, Random close packing of disks and spheres in confined geometries, Phys. Rev. E **80**, 051305 (2009).
- [76] E. Bernard, W. Krauth, and D. Wilson, Event-chain Monte Carlo algorithms for hard-sphere systems, Phys.

- Rev. E. **80**, 056704 (2009).
- [77] M. Michel, S. Kapfer, and W. Krauth, Generalized event-chain Monte Carlo: Constructing rejection-free global-balance algorithms from infinitesimal steps, *J. Chem. Phys.* **140**, 054116 (2014).
- [78] T. Grigera and G. Parisi, Fast Monte Carlo algorithm for supercooled soft spheres, *Phys. Rev. E* **63**, 045102 (2001).
- [79] L. Berthier, D. Coslovich, A. Ninarello, and M. Ozawa, Equilibrium sampling of hard spheres up to the jamming density and beyond, *Phys. Rev. Lett.* **116**, 238002 (2016).
- [80] F. Ghimentì, L. Berthier, and F. van Wijland, Irreversible Monte Carlo algorithms for hard disk glasses: from event-chain to collective swaps, *Phys. Rev. Lett.* **133**, 028202 (2024).
- [81] C. Rycroft, G. Grest, J. Landry, and M. Bazant, Analysis of granular flow in a pebble-bed nuclear reactor, *Phys. Rev. E* **74**, 021306 (2006).
- [82] C. Rycroft, *Multiscale modeling in granular flow*, Ph.D. thesis, Massachusetts Institute of Technology, Department of Mathematics (2007).
- [83] H. Nematì and J. de Graaf, The Cellular Potts Model on Disordered Lattices, *Soft Matter* **accepted**, 1 (2024).
- [84] H. Zhu, S. Thorpe, and A. Windle, The geometrical properties of irregular two-dimensional Voronoi tessellations, *Phil. Mag. A* **81**, 2765 (2001).
- [85] M. Tanemura, Statistical distributions of Poisson Voronoi cells in two and three dimensions, *Forma* **18**, 221 (2003).
- [86] D. Morley and M. Wilson, Voronoi diagrams in quasi-2D hard sphere systems, *J. Stat. Mech.* **2020**, 093201 (2020).
- [87] A. Bug, S. Safran, G. Grest, and I. Webman, Do interactions raise or lower a percolation threshold?, *Phys. Rev. Lett.* **55**, 1896 (1985).
- [88] Small departures are expected as the two sizes of colloids used have a little polydispersity and the smaller colloids can be slightly beneath the larger colloids, as their center of mass can be closer to the substrate.
- [89] A. Huerta, A. Carrasco-Fadanelli, and A. Trokhymchuk, Towards frustration of freezing transition in a binary hard-disk mixture, *Condens. Matter Phys.* **15**, 43604 (2012).
- [90] C. Bennett and B. Alder, Studies in molecular dynamics. IX. Vacancies in hard sphere crystals, *J. Chem. Phys.* **54**, 4796 (1971).
- [91] Note that P_5^* is a positive number always, hence the cusp is not a sign of a number going through zero, as is often found in logarithmic representations where the absolute of a value is plotted.
- [92] V. Senthil Kumar and V. Kumaran, Voronoi cell volume distribution and configurational entropy of hard-spheres, *J. Chem. Phys.* **123**, 114501 (2005).
- [93] E. Corwin, M. Clusel, A. Siemens, and J. Bruijic, Model for random packing of polydisperse frictionless spheres, *Soft Matter* **6**, 2949 (2010).
- [94] C. Oâ€™Donovan, E. Corwin, and M. Möbius, Mean-field granocentric approach in 2D & 3D polydisperse, frictionless packings, *Phil. Mag.* **93**, 4030 (2013).
- [95] S. Hilgenfeldt, Size-topology correlations in disk packings: terminal bidispersity in order–disorder transitions, *Phil. Mag.* **93**, 4018 (2013).
- [96] A. Donev, F. Stillinger, and S. Torquato, Configurational entropy of binary hard-disk glasses: Nonexistence of an ideal glass transition, *J. Chem. Phys.* **127** (2007).
- [97] This observation does *not* conflict with the fact that in Fig. 2a-c, I observe dips in the $P_\phi(q)$ about integer values of n_q and a smooth increasing trend near half-integer values of n_q . There is a bias to the representation of the system using $P_\phi(q)$, as explained in Section IV.
- [98] S. Hermann and M. Schmidt, Noether’s theorem in statistical mechanics, *Commun. Phys.* **4**, 176 (2021).
- [99] L. Oswald, S. Grosser, D. Smith, and J. Käs, Jamming transitions in cancer, *J. Phys. D.* **50**, 483001 (2017).
- [100] M. Spencer, Z. Jabeen, and D. Lubensky, Vertex stability and topological transitions in vertex models of foams and epithelia, *Euro. Phys. J. E* **40**, 1 (2017).
- [101] H. Jain, A. Voigt, and L. Angheluta, Robust statistical properties of T1 transitions in a multi-phase field model of cell monolayers, *Sci. Rep.* **13**, 10096 (2023).
- [102] D. Krommydas, L. Carenza, and L. Giomi, Collective epithelial migration is mediated by the unbinding of hexatic defects, *arXiv* **2307.12956**, 1 (2023).
- [103] N. H. Barbhuiya and C. K. Mishra, Anisotropic cage evolution in quasi-two-dimensional colloidal fluids, *arXiv* **2407.18032**, 1 (2024).
- [104] N. Claussen and F. Brauns, A Mean-Field Model for Active Plastic Flow of Epithelial Tissue, *arXiv* **2409.13129**, 1 (2024).
- [105] L. Boué, E. Lerner, I. Procaccia, and J. Zylberg, Predictive statistical mechanics for glass forming systems, *J. Stat. Mech.* **2009**, P11010 (2009).
- [106] W. Kauzmann, The nature of the glassy state and the behavior of liquids at low temperatures, *Chem. Rev.* **43**, 219 (1948).
- [107] C. Royall, F. Turci, S. Tatsumi, J. Russo, and J. Robinson, The race to the bottom: approaching the ideal glass?, *J. Phys.: Cond. Mat.* **30**, 363001 (2018).
- [108] V. Bolton-Lum, R. Dennis, P. Morse, and E. Corwin, The Ideal Glass and the Ideal Disk Packing in Two Dimensions, *arXiv* **2404.07492**, 1 (2024).
- [109] H.-B. Yu, L. Gao, J.-Q. Gao, and K. Samwer, Universal origin of glassy relaxation as recognized by configuration pattern matching, *Nat. Sci. Rev.* **11**, nwae091 (2024).
- [110] L. Silbert, Jamming of frictional spheres and random loose packing, *Soft Matter* **6**, 2918 (2010).
- [111] E. Hinrichsen, J. Feder, and T. Jøssang, Random packing of disks in two dimensions, *Phys. Rev. A* **41**, 4199 (1990).
- [112] M. Ciamarra and A. Coniglio, Random very loose packings, *Phys. Rev. Lett.* **101**, 128001 (2008).
- [113] M. Merkel and M. Manning, A geometrically controlled rigidity transition in a model for confluent 3D tissues, *New J. Phys.* **20**, 022002 (2018).
- [114] G. Onoda and E. Liniger, Random loose packings of uniform spheres and the dilatancy onset, *Phys. Rev. Lett.* **64**, 2727 (1990).
- [115] D. Sussman and M. Merkel, No unjamming transition in a Voronoi model of biological tissue, *Soft Matter* **14**, 3397 (2018).
- [116] It is nearly inevitable that a literature reference has been missed and I apologize should your work unwittingly not receive the same attention as those listed in this section.
- [117] A. Chieco, M. Zu, A. Liu, N. Xu, and D. Durian, Spectrum of structure for jammed and unjammed soft disks, *Phys. Rev. E* **98**, 042606 (2018).

- [118] S. Atkinson, F. Stillinger, and S. Torquato, Existence of isostatic, maximally random jammed monodisperse hard-disk packings, *Proc. Natl. Acad. Sci.* **111**, 18436 (2014).
- [119] D. Koeze, D. Vågberg, B. Tjøa, and B. Tighe, Mapping the jamming transition of bidisperse mixtures, *Europhys. Lett.* **113**, 54001 (2016).
- [120] M. Maiti and M. Schmiedeberg, The thermal jamming transition of soft harmonic disks in two dimensions, *Euro. Phys. J. E* **42**, 1 (2019).
- [121] D. Bideau, A. Gervois, L. Oger, and J. Troadec, Geometrical properties of disordered packings of hard disks, *J. Phys.* **47**, 1697 (1986).
- [122] J. Berryman, Random close packing of hard spheres and disks, *Phys. Rev. A* **27**, 1053 (1983).
- [123] K. Strandburg, Two-dimensional melting, *Rev. Mod. Phys.* **60**, 161 (1988).
- [124] U. Gasser, Crystallization in three- and two-dimensional colloidal suspensions, *J. Phys.: Cond. Mat.* **21**, 203101 (2009).
- [125] S. Kapfer and W. Krauth, Two-dimensional melting: From liquid-hexatic coexistence to continuous transitions, *Phys. Rev. Lett.* **114**, 035702 (2015).
- [126] N. I. Lebovka, M. R. Petryk, and N. V. Vygornitskii, Percolation connectivity in deposits obtained using competitive random sequential adsorption of binary-disk mixtures, *Cond. Mat. Phys.* **27**, 13201 (2024).
- [127] E. Zaccarelli, S. Liddle, and W. Poon, On polydispersity and the hard sphere glass transition, *Soft Matter* **11**, 324 (2015).
- [128] J. Geiger, N. Grimm, M. Fuchs, and A. Zumbusch, Decoupling of rotation and translation at the colloidal glass transition, *J. Chem. Phys.* **161**, 014507 (2024).
- [129] B. Grünbaum and G. C. Shephard, Tilings with congruent tiles, *Bull. Amer. Math. Soc.* **3**, 951 (1980).
- [130] W. Götze, J. Hansen, D. Levesque, and J. Zinn-Justin, *Liquids, freezing and the glass transition* (Amsterdam, Netherlands, 1991) p. 287.

Appendix A: Comparison to the Literature

My study into the dynamics and structure of 2D bidisperse disks builds on decades of research into the structure and dynamics of dense (quasi-)2D suspensions. In this appendix, I will compare my results to those obtained in the literature, where I aim to be as extensive as possible [116]. Again, referencing the R - ϕ diagram of Fig. 4, I have put (estimated) data points from the literature on top of my results, labeling these “a” through “q”.

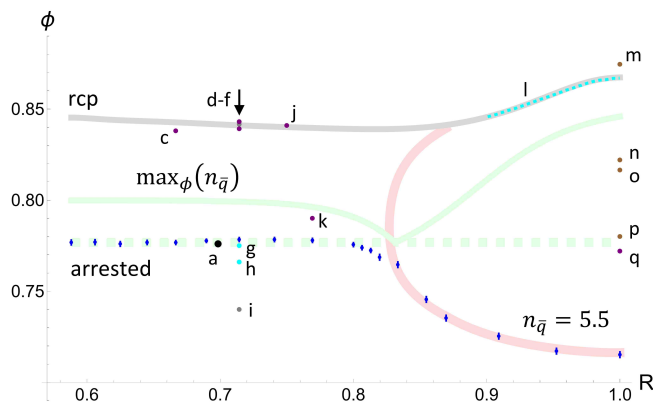


FIG. 8. **Comparison to the literature.** The R - ϕ state diagram for bidisperse disks in 2D is the same as in Fig. 4a. The dots marked with letters (“a”-“q”; “l” corresponds to the dashed cyan curve) indicate systems for which literature values are known. The large black point “a” represents the experimental system of interest [1] as before. The purple points indicate systems that can be directly mapped to my simulations. Cyan data points represent comparable systems, for which some interpretation of the mapping is required. Brown points follow from theoretical calculations and gray points represent systems that may be compared to my data, but for which the translation is not necessarily obvious. The text in this appendix provides the details on all comparisons and how to interpret these.

Point “a” is the experimental reference [1]. Point “b” is omitted, as I previously discussed this in Fig. 5 and this falls outside of the ϕ range shown here. There is also a point “r”, which is discussed in Appendix C, and not shown here to keep the presentation clean. I will now go over these points and discuss how they were obtained and what can be learned from the comparison.

Points “c”-“f”, “j”, “l”, and “m” relate to the rcp value ϕ_m obtained using the algorithm of Ref. [75]. The first point, labelled “c”, was obtained from the experimental study of Zhao *et al.* [45], wherein the two-point correlation of free Voronoi volumes in binary disc packings was measured. The size ratio of their teflon disks is 6 mm to 9 mm, which results in $R \approx 0.67$. The authors report a maximum value of $\phi = 0.838$ for their packing, which is in good agreement with the rcp value that I determined.

From top to bottom, points “d” through “f” correspond to data with $R^{-1} = 1.4$ that was obtained from Refs. [110]

($\phi \approx 0.843$), [117] ($\phi \approx 0.8416$), and [118] ($\phi \approx 0.8391$), respectively. The top data point derives from a numerical study into the effect of friction on the jamming properties of disordered particle packings of bidisperse disks [110]. This point was obtained in the frictionless limit, which is appropriate here. The middle data point was extracted from a study of 50:50 bidisperse harmonically repulsive disks with 7:5 diameter ratio [117]. Here, I present the fitted value of the jamming fraction as extracted in Appendix B2 of their work. Note that despite the softness of the potential this extracted jamming point agrees very well with my rcp value. Lastly, the bottom data point specifically examines isostatic, maximally random jammed monodisperse hard-disk packings [118]. This point too matches my ϕ_m value well, which is expected for a study into jamming.

The point labelled “j”, derives from Ref. [54]. Rieser *et al.* considered the divergence of Voronoi cell anisotropy vector for both experimental and numerical data on bidisperse disk-like packings [54]. Here, I take the value $\phi \approx 0.8409$ that was obtained using their quenched simulation protocol for $R = 0.75$; the ϕ for their thermalized data point ($\phi \approx 0.8465$) agreed less well with my rcp value. It may be that thermalization makes the softness of the simulated particles play a more significant role.

The curve labelled “l”, was obtained from Ref. [119], which systematically mapped out the jamming transition of all 2D bidisperse mixtures of frictionless disks in the hard particle limit. In particular, I extracted the data from their Fig. 8 for the largest number of particles simulated and interpolated this to arrive at the dashed cyan curve. Finally, point “m” comes from Ref. [26], wherein a theory of amorphous packings and more generally glassy states of hard spheres is reviewed. Their Table III reports a 2D value of $\phi \approx 0.8745$ that follows from a first-order small cage expansion of the ‘glass close-packing’ density. The agreement is reasonable given the nature of the theoretical approximation employed in Ref. [26].

I conclude that the rcp values obtained using algorithm of Desmond and Weeks [75] agree well with the various pieces of (more modern) literature. Note that I also already commented on the excellent agreement between my numerical result and the experimentally obtained value of ϕ for which the SISF relaxation time diverges [1] in Section V. All of this together provides confidence in my choice of setting ϕ_m as an upper bound to the considered ϕ range.

Next, let us cover points “i”, “n”, and “o”, which do not appear to match any feature in the state diagram, before moving onto a discussion of the remaining points that do. Point “i” derives from a numerical study of bidisperse systems ($R^{-1} = 1.4$) comprising soft harmonic disks in 2D [120]. The authors report a “thermal jamming transition”, wherein at $\phi \approx 0.74$ an effectively non-ergodic state sets in for which there remain overlaps. The application of this result to the hard-disk packings I have studied is slightly tenuous, however, their ϕ value approaches where I place the onset of apparent arrested dynamics. That being said, it much more closely matches the $n_p = 5.5$ percolation value discussed in Appendix D (not shown here). Thus, there is no obvious conclusion that can be drawn from perceived agreement and any correspondence is more than likely a fortuitous coincidence.

Point “n” was obtained from the combined theoretical and experimental work of Ref. [121], wherein an approximate expression for the close-packing density $\phi \approx 0.822$ of a monodisperse sample is proposed. Clearly, the point deviates considerably from the rcp value obtained here, though it agrees with a previous experimental study to within the error [122]. I have nonetheless included this point, as the theory put forward in this source was used to obtain a data point (“p”) that agrees better with one of my measures. Lastly, point “o” follows from the theory of Ref. [26] (see their Table III), and is identified as the point where a thermodynamic glass transition is supposed to happen. Within the limitations of my analysis, I find no evidence for this transition. However, I should stress that I did not pursue analysis of the ideal glass transition; if it is even present for a monodisperse system [96].

This leaves points “g”, “h”, “k”, “p”, and “q”. The first, point “g”, follows from Ref. [96], wherein a binary hard-disk mixture is studied with ratio of disk diameters $R^{-1} = 1.4$. The authors report $\phi \approx 0.775$ for the (equilibrium) freezing area fraction. However, this study was performed for a 1:2 stoichiometric ratio of large to small disks. I will argue in Section VIII how this fits my interpretation of ϕ_a .

Next, point “h” follows from Ref. [110], which studied frictional hard-disks with $R^{-1} = 1.4$. Here, I fitted the jamming data points with a sigmoidal curve and extrapolated to the infinite friction result to a rlp value of $\phi \approx 0.766$. The reason for taking this fitting approach is that Silbert does not report the 2D jamming value. Moreover, there is a peculiar nonmonotonicity to the coordination-number data for 2D systems provided in Table I of Ref. [110]. Given the level of uncertainty on the data provided, the agreement between my fitted rlp value of $\phi \approx 0.766$ and the arrested-dynamics area fraction ϕ_a obtained in this study is very good. It is curious that there appears to be a connection between rlp of a fully frictional sample and the apparent arrested dynamics in a frictionless system. My interpretation is that this is another signal of an underlying geometric feature, see Section VIII.

Point “k” was obtained from Ref. [53], the authors of which took a very similar approach to studying 2D systems with arrested dynamics. They considered the evolution of Voronoi cell geometry in simple hard-disk models by simulations and colloid experiments. In particular, they located the ‘glass transition’ using a Voronoi-based (neighborhood) cage anisotropy parameter. Their anisotropy takes the ratio of the long and short axes of the Voronoi cells and has a peak similar to what I find when studying $\max_{\phi}(n_{\bar{q}})$. Here, I use their point $\phi \approx 0.79$ which was obtained *via* 2D EDMD of bidisperse disks with $R^{-1} = 1.3$ and a 50:50 number ratio. This data point is in good agreement with where I locate

ϕ_a and $\max_\phi(n_{\bar{q}})$, respectively, given the subtle differences in approach and the uncertainty this imposes. However, based on my analysis, a change in cage anisotropy does not fully coincide with the apparent kinetic arrest, though it is possible that a measure based on aspect ratio, as pursued in Ref. [53], leads to a closer connection.

Reference [111] makes use of the theory by Bideau *et al.* [121] to predict the rlp density of $\phi \approx 0.78$, which is indicated by point “p”, for a monodisperse sample of hard disks. The point “q” follows from the numerical study performed in the same paper, which places the rlp area fraction at $\phi \approx 0.772$. Given the limitations of this study, the agreement with the dashed green line, and thus the minimum in the amount of pentagonal large-particle neighborhoods, is excellent. This is a second piece of evidence — also see point “h” above — in the direction of geometric features underlying the $\phi \approx 0.777$ line in the systems considered in my research. Note that Ref. [111] reports on an average number of contacts per disk being ≈ 3 at their rlp ϕ . Using my Voronoi approach, I find an average number of neighbors that is substantially larger, see Fig. 2d. It is, however, interesting to assess how many of these neighbors contribute to ‘immobilizing’ contacts, such as considered in Ref. [111], at any one time.

Appendix B: Pseudo-Polygon Fractions

In the main text, I analyze features of $P_\phi(q)$, see Fig. 2, to establish features of the state diagram, see Fig. 4. One aspect of this analysis is the crossover between the highest mode (of the PDF) being pentagonal to hexagonal, see Fig. 5. This may give the false impression that the system transitions from being mostly pentagonal to mostly hexagonal, *i.e.*, undergoes a disordered-to-ordered transition. Here, I therefore examine the fraction of pseudo-polygons, see Fig. 9, which shows the fraction of pseudo- n -gons f_n as a function of the area fraction ϕ .

My study of the fraction of pseudo-polygons reveals that for low ϕ , there is an abundance of low- n neighborhoods, *i.e.*, pseudo-triangles and -squares. This makes sense, as the neighborhoods are relatively independent of the particle shape. As ϕ increases, the fraction of pseudo-pentagons and pseudo-hexagons rises. The first takes over in highest abundance at $\phi \approx 0.5$, while the latter can become the dominant shape for sufficiently high values of R only. I further note that as ϕ increases to its rcp value ϕ_m , any trend of increase in f_n transitions toward one of decrease and *vice versa*. This can be explained by the fact that in order to compact the system maximally in the square simulation boxes that I used throughout the study, defects must be introduced for the hexagonal crystal structures. The situation is less clear cut for the systems that (appear) to remain amorphous. This lowers the abundance of the prevalent pseudo-polygon and can increase fractions of less abundant neighborhood shapes.

For $R^{-1} > 1.35$ (equivalently $R \lesssim 0.74$), I find that there for all ϕ I have $f_6 < f_5$ (vertical dotted purple lines in Fig. 9). Note that $R \approx 0.74$ is not value for which the $n_{\bar{q}} = 5.5$ curve closes in on itself, which occurs for $R \approx 0.83$. Thus, there is no transition from pentagonal to hexagonal below $R \approx 0.74$, which presumably changes the behavior of the system from being polycrystalline to being truly disordered. However, as is evidenced by the neighborhood composition graphs in Fig. 9, the system takes on a range of compositions as a function of ϕ even for relatively low R . So one has to be careful in drawing to strong conclusions based on Fig. 9.

Lastly, Fig. 9 visualizes where there is kinetic arrest using a vertical solid purple line. In panels (a) and (b), there appears to be a subtle kink in the $n = 6$ and $n = 5$ data, respectively, where I locate ϕ_a . However, also considering the other data, I was unable to find an obvious feature to the fraction of pseudo- n -gons data that correlates with the apparent kinetic arrest. If it is present in this data, it is merely a subtle effect.

Appendix C: Pressure

Throughout this paper, I have considered the system in the NVT ensemble (technically at constant area). There is coexistence between a disordered fluid, hexatic phase, and hexagonal crystal at values of $R \approx 1$. Given the system size that I considered, picking up on the hexatic phase is not realistic [123–125]. However, I should still find the features of a first-order transition between a disordered fluid and ordered hexagonal phase in my data. One such feature is the presence of a van-der-Waals loop in the pressure p as a function of the inverse particle density $v = V/N = \rho^{-1}$. I therefore computed the pressure from the collisions in the system *via* the momentum exchange during collisions, using the standard virial expression. This was averaged and subsequently used to establish van-der-Waals loops whenever they are present, see Fig. 10a for an example.

For sufficiently low values of R , *i.e.*, values of the size ratio below $R \approx 0.87$, I was unable to detect a loop structure. However, my data was still of sufficient quality to establish a minimum slope. That is, as the loop vanishes, there is an inflection point, suggestive of a critical point, see Fig. 10b. Lowering R further (up to $R \approx 0.82$), I still observe a change in slope, see Fig. 10c, for which I can determine the value of v (or equivalently ϕ) where the slope attains a local minimum. Figure 10d shows the coexistence points and local minima obtained using the pressure curves on

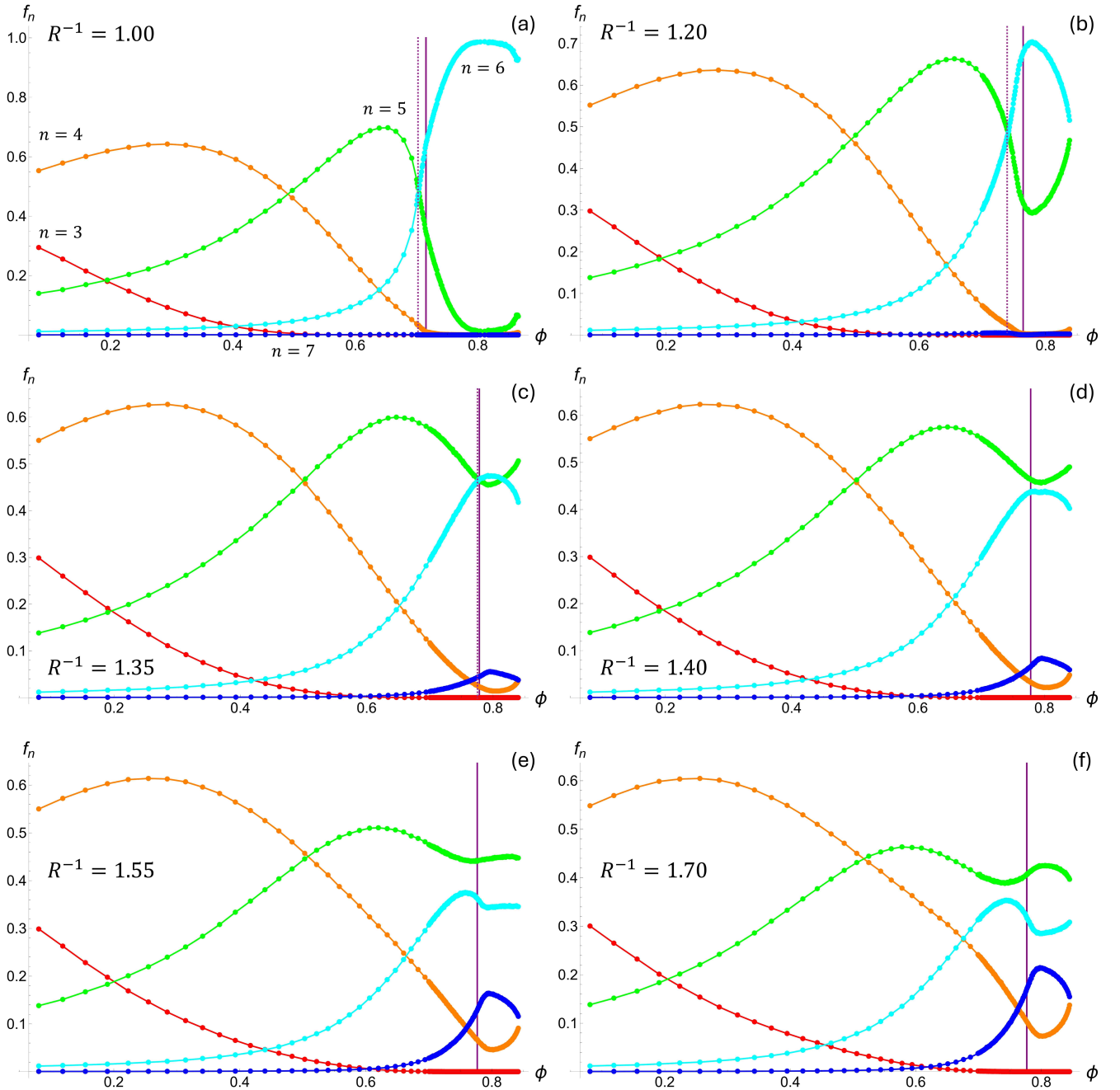


FIG. 9. **Fractions of pseudo-polygons in the sample.** (a-f) The fraction f_n of pseudo-triangles (red, $n = 3$), -squares (orange, $n = 4$), -pentagons (green, $n = 5$), -hexagons (cyan, $n = 6$), and -heptagons (blue, $n = 7$), as a function of the area fraction ϕ . The dots show the sampling points, and the curves are guides to the eye that connect these. The relevant inverse size ratio R^{-1} is indicated in each panel. The vertical solid purple line indicates the value of ϕ for which the system falls out of equilibrium, ϕ_a , *i.e.*, where the extrapolated diffusion coefficient vanishes. The vertical dotted purple line indicates the value of ϕ for which there is a larger fraction of pseudo-hexagons than there is of pseudo-pentagons.

top of the state diagram from Fig. 4. I observe that for R close enough to 1 the top coexistence curve matches the pseudo-polygon curve $n_{\bar{q}} = 5.5$ quite well.

I also compared my coexistence data to that reported in the literature [89], which was obtained using a standard Monte Carlo simulation technique based on the Metropolis algorithm. The number of particles considered in this study is smaller (400), yet I observe an acceptable agreement between their results and mine for $R \approx 1$. For lower R , I do not pick upon coexistence, presumably because there is a difference in the level of equilibration. Note that

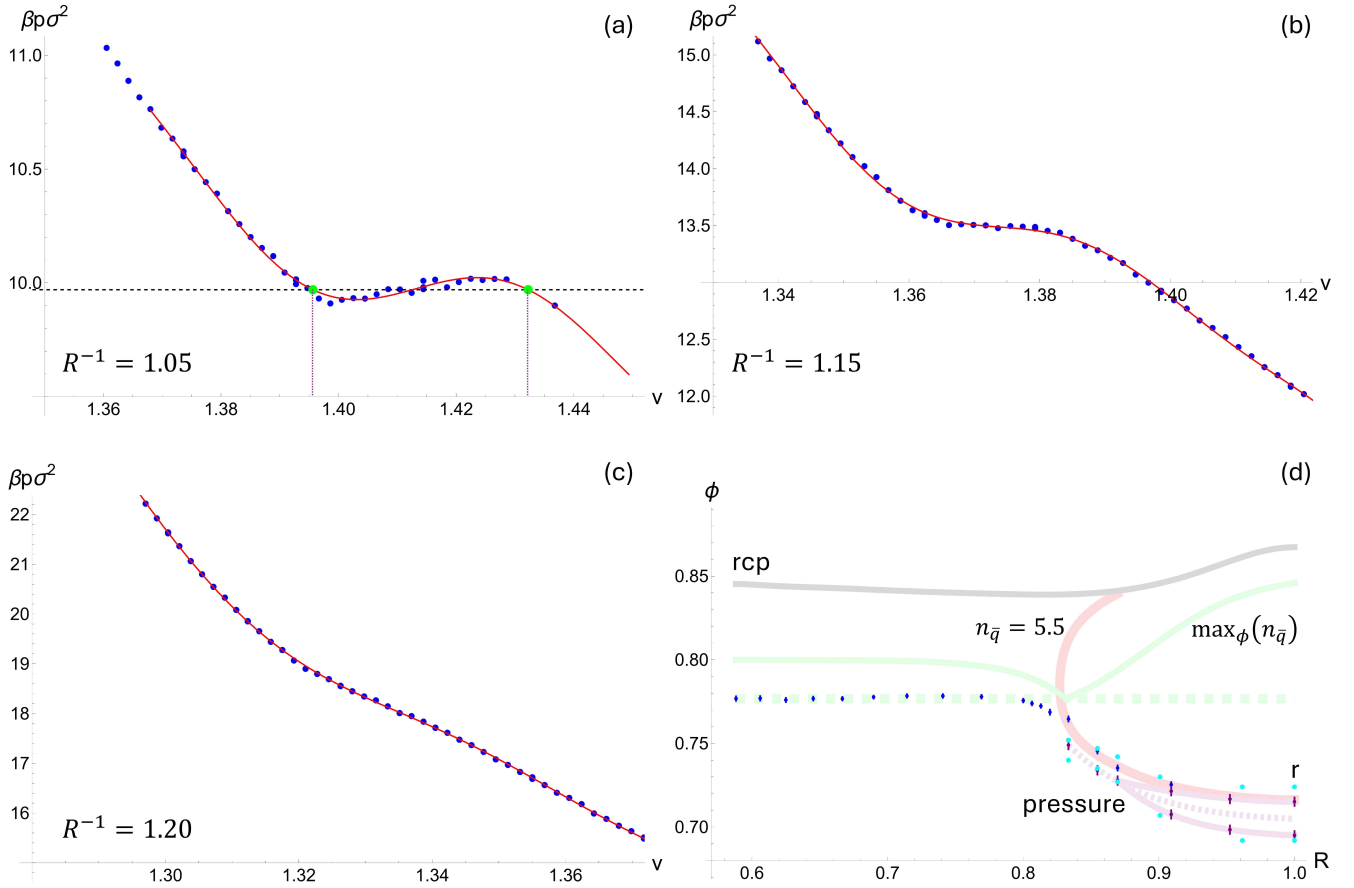


FIG. 10. **Determining the phase transition by measuring the pressure.** (a-c) Pressure curves (blue points) showing the reduced pressure $\beta p \sigma^2$ — β is the inverse thermal energy and σ is the diameter of the largest particle — as a function of the inverse particle density $v = V/N = \rho^{-1}$. The relevant size ratio R is provided in the bottom-left corner of the graphs. The red curves represent polynomial fits to the data. (a) This graph shows a clear van-der-Waals loop for which the coexistence pressure is indicated by the horizontal dashed black line. The two extracted coexistence points are indicated in green and the associated v using vertical dotted purple lines. (b) This graph shows an inflection point, but no longer a van-der-Waals loop. (c) The $R^{-1} = 1.2$ data still has a change in slope, for which the minimum slope can be fitted. (d) The R - ϕ state diagram of Fig. 4 with the ϕ for which there is dynamic arrest indicated in blue. On top of this, I have added the pressure data extracted from the van-der-Waals loops and changes in slope in purple. The solid purple curves guide the eye for the coexistence area fractions, while the dashed purple curve guides the eye for the minimum-slope data below $R \approx 0.87$. Below $R \approx 0.82$ I was unable to accurately determine any such minimum. Error bars denote the standard error of the mean in all cases. The cyan data points labelled “r” are obtained from Ref. [89], wherein coexistence ϕ and p were determined.

obtaining coexistence was not the aim of this study nor is it easy to compare Monte Carlo and EDMD directly.

Appendix D: Shell and Shape Percolation

I desired to confirm the nearly constant value of ϕ_a in the range $R \lesssim 0.8$, also see Fig. 4. In order to independently measure this, I considered percolation in the system. It should be clear that when working with hard particles, contact percolation only occurs at rcp. However, when there is a substantial structural change or the system falls out of equilibrium there should be a change in the number of collisions. As the temperature — the average particle velocity — is maintained constant, physical intuition suggests that the gaps between particles should reflect such a change in collision rate. In post-processing the data, I analyzed this as follows.

I augmented the size of each particle with a small shell of size ϵ , that is, when particle i has a diameter σ_i , I treat it as having a diameter $\sigma_i + 2\epsilon$, see Fig. 11a. I use a cluster algorithm to identify the largest cluster and establish whether the system is percolating by checking whether it spans the simulation box in both directions [87, 126], see the ESI [59] for the code. This is done over all realizations of the system at a given R and ϕ value.

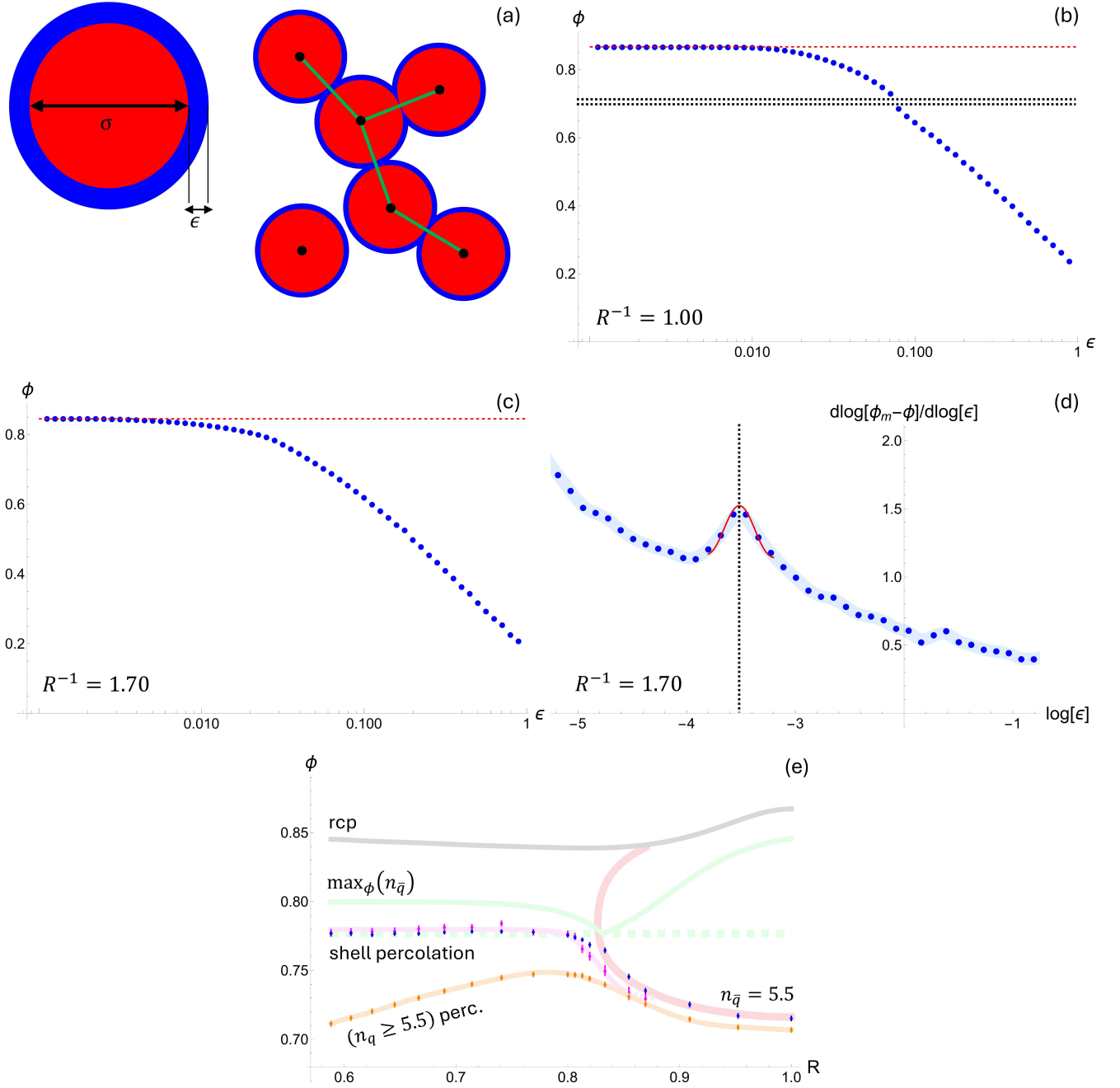


FIG. 11. **Percolation transitions based on contact and isoperimetric quotient.** (a) Illustration of the shell-based percolation procedure. Each hard-disk particle (red) with diameter σ is surrounded by a shell (blue) of width ϵ , which does not impact the interactions. These shells are used to determine local clusters, as illustrated for a small cluster of four particles using green lines. Note here I only show a monodisperse example, but the procedure is equivalent for a bidisperse system. (b,c) The value of the area fraction ϕ for which the percolation transition occurs as a function of the shell width in log-linear representation. The dashed red line indicates the asymptotic value for ϕ when $\epsilon \downarrow 0$, which corresponds to the rcp value ϕ_m shown in Fig. 4. In panel (b), the system is monodisperse ($R = 1$) and there appear to be two branches to the curve, as indicated using the dotted black lines, which guide the eye. In panel (c), the system is bidisperse with an inverse size ratio $R^{-1} = 1.7$. Note that the curve appears relatively smooth. (d) Approach to finding the value of ϵ for which the system changes. The curve shows the numerically computed value of $(\partial \log[\phi_m - \phi]) / (\partial \log \epsilon)$, which shows a clear peak near $\log \epsilon = -3.5$. This peak is fitted using a fourth-order local polynomial fit (red curve) and used to establish the ϵ value for which the system undergoes a change, ϵ^* , as indicated using the dotted black line. (e) Representation of the R - ϕ diagram in Fig. 4, which shows the ϕ^* following from the shell percolation ϵ^* in magenta. The blue data shows the kinetic arrest obtained from the MSDs. Another form of percolation was considered by establishing when a system-spanning cluster of local neighborhoods with $n_q \geq 5$ was obtained (orange data). That is, a cluster of particles whose neighborhood is closer to being hexagonal than it is to being pentagonal. The dots indicate the data, the error bars show the standard error of the mean, and the curves guide the eye.

I then use this data to establish a fraction of times that the system is clustered. Between $\phi = 0$ and the rcp value ϕ_m , I always find some fraction of the systems to clusters and this ϕ dependence can be fitted accurately using a sigmoid, see the ESI [59]. The mid-point of the sigmoid is used to establish the percolation area fraction $\phi(\epsilon)$, as shown in Fig. 11b,c. The idea is that in the limit of an infinite system size, the sigmoid becomes a Heaviside function about the percolation ϕ .

It is clear that the percolation area fraction tends asymptotically toward the rcp value ϕ_m for $\epsilon \downarrow 0$. Additionally, as $\epsilon \uparrow \infty$, I have that $\phi(\epsilon) \downarrow 0$. Interestingly, I see that there are two branches to this shell-percolation ϕ when the system undergoes a (first-order) phase transition from a disordered fluid to a hexagonal crystal, see Fig. 11b for $R = 1$. While the two branches are visually obvious, it proved difficult to fit the end points of the two branches with sufficient accuracy. That is, determining the associated value of ϵ and then inferring coexistence ϕ should be possible. However, given the number of numerical operations carried out to arrive at $\phi(\epsilon)$, it is difficult to obtain a precise ϕ value from an ϵ with significant variance.

The data appears more smooth when the system does not seem to undergo a first-order phase transition, see Fig. 11c for $R^{-1} = 1.7$. However, given the quality of the data it is not possible to state definitively whether the curve is smooth or that there remains a small gap, as was the case for $R = 1$. Nonetheless, it is possible to extract the ϕ_a from this seemingly smooth percolation line. I measured the distance to ϕ_m and take the natural logarithm of this separation ($\phi_m - \phi$) as well as that of ϵ .

From this data I can numerically determine the local power-law exponent $(\partial \log [\phi_m - \phi]) / (\partial \log \epsilon)$, using a simple central differences scheme. This local power-law exponent exhibits a clear peak, see Fig. 11d, which can be fitted using a fourth-order polynomial $a + b \log^2 \epsilon + c \log^4 \epsilon$ (red curve). The peak position ϵ^* in turn can be used to establish the position of the peak $\phi(\epsilon^*)$. Note that this position corresponds to a change in slope in the original $\phi(\epsilon)$ data, which is what I sought to locate.

The corresponding area fraction is shown in Fig. 11e for those points where there was no clear indication that there were two branches (magenta data). It is directly apparent that the data accurately fits ϕ_a (blue data) for $R \lesssim 0.80$. For the remaining range, $R \gtrsim 0.81$, the trend is more close to the one of the $n_{\bar{q}} = 5.5$ curve (red).

Lastly, I studied whether there was any significance to shape percolation. That is, I note that crystallization is accurately predicted using $n_{\bar{q}} = 5.5$, but that this is a poor predictor of ϕ_a . Therefore, I sought to establish those ϕ for which percolation is obtained when particles are added to a cluster whenever $n_q \geq 5.5$. This data is shown using orange in Fig. 11e. The last bit of the guide to the eye is dashed because it was not clear whether there was a branched or a continuous $\phi(\epsilon)$ curve. For $R \gtrsim 0.83$, the curve lies half-way between the two coexistence values of ϕ as established using the pressure calculation in Fig. 10. These are not shown here to avoid cluttering the figure. I conclude that there is limited value to this measure.

Appendix E: Median Isoperimetric Quotient

I have shown that the system crystallizes at $n_{\bar{q}} = 5.5$. However, a connection between *global* properties of the neighborhood distribution and ϕ_a was less readily apparent.

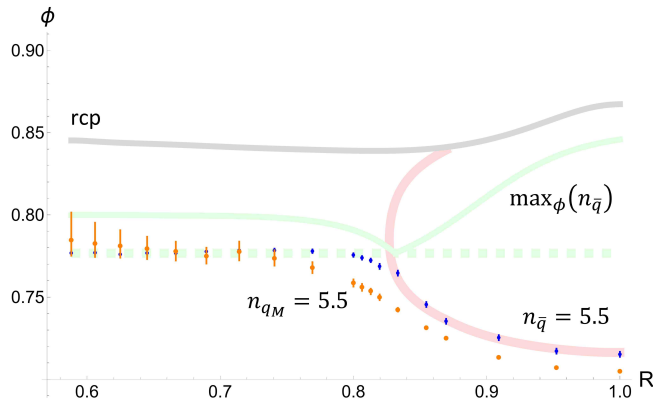


FIG. 12. **Properties of the median of the isoperimetric quotient distribution.** The values of ϕ for which the median to $P_\phi(q)$, q_M , has $n_{q_M} = 5.5$ (orange). This data is presented on top of a part of the R - ϕ state diagram of Fig. 4. The error bars indicate the standard error of the mean, which here is asymmetric.

Here, I therefore consider the median of $P_\phi(q)$, q_M , which is the q value that splits PDF into two parts of equal

area. This choice is further motivated by the various fraction of pseudo-polygons reported in Appendix B. In Fig. 12, I show those values of ϕ , for which $n_{q_M} = 5.5$. Because of the error on the isoperimetric-quotient distribution, there is a sizeable level of uncertainty when it comes to the placement of the median-derived ϕ value, see the ESI [59] for additional details. However, note that for $R \lesssim 0.72$ there is reasonable agreement between the ($n_{q_M} = 5.5$) area fraction and ϕ_a for arrested dynamics, given the uncertainty in the data.

Appendix F: Perspective on 3D Hard-Sphere Systems

Let us attempt to apply the notion of a geometric ground state to 3D hard-sphere systems, for which the volume fraction η is the control parameter. No experiments similar to the ones performed by Lozano *et al.* [1] and Li *et al.* [2] have been performed in 3D to the best of my knowledge. Given that Lozano *et al.* placed the glass transition at $\phi \approx \phi_g \approx 0.777$, it makes sense to try to connect to observations on the 3D glass transition. Acknowledging that the dynamics in 3D may be very different from 2D, this at least provides a reference point.

The literature places the hard-sphere glass-transition across a wide range of η close to $\eta = 0.6$. For example, Zaccarelli *et al.* [127] provide $\eta_g \approx 0.588$ for the smallest spheres in a polydisperse sample. A recent work by Geiger *et al.* [128] on a bidisperse sphere mixture places the transition at $\eta_g \approx 0.61$. Given that my 2D results are obtained for bidisperse systems, the value of $\eta_g = 0.61$ will serve as my reference point.

I start by assuming that I can focus on monodisperse spheres that are arranged in such a way that their Voronoi cells tile space, drawing the analogy to my findings in 2D. Elements of a subclass of space-filling polyhedra, referred to as plesiohedra [129], meet this requirement. Among these, cubic Voronoi cells are obtained for a simple-cubic lattice with $\eta = \pi/6$. Truncated-octahedron-shaped Voronoi cells correspond to a body-centered cubic arrangement (bcc) with $\eta = \sqrt{3}\pi/8$. The face-centered cubic (fcc) arrangement has Voronoi cells shaped like a rhombic dodecahedron and $\eta = \pi/\sqrt{12} \approx 0.9069$. Spheres arranged in a hexagonal close packing (hcp) also have $\eta = \pi/\sqrt{12}$, but their Voronoi cell is a trapezo-rhombic dodecahedron has two types of faces.

Removing the central particle out of a neighborhood in an fcc arrangement, gives a volume fraction $\eta = \pi\sqrt{12}/13 \approx 0.8371$ and associated Voronoi cells that are rhombic dodecahedron with one face extended into a point. Removing a central particle in an hcp arrangement will give two types of Voronoi cell, as the base is a trapezo-rhombic dodecahedron, which has both trapezoids and rhombi as its sides. None of these elements have a volume fraction that convincingly matches η_g . Turning to the bcc lattice, I also gain two types of Voronoi cell by removing the ‘body’ from the body-centered cubic arrangement. There are 6 next-nearest neighbors for which the square face is extended, leading to a Voronoi cell with $\eta = 6\sqrt{3}\pi/49 \approx 0.666294$. Additionally, there are 4 nearest neighbors for which the hexagonal face is extended, and I find $\eta = 4\sqrt{3}\pi/35 \approx 0.621874$. This is relatively close to the reported value of η_g , but the connection is not strong. Potentially one could take the mean of the two and obtain a value $\eta \approx 0.644$ that is close to the random-close packing value for hard spheres in 3D [122]. Though this is highly speculative.

A simple cubic arrangement of particles gives $\eta = \pi/6 \approx 0.52360$, which significantly underestimates the transition value, placing it closer to the prediction ($\eta \approx 0.52$) of mode-coupling theory [130]. Lastly, I consider the triakis truncated tetrahedron, which is generated by the diamond lattice. This polyhedron tiles space and gives rise to $\eta = \sqrt{3}\pi/16 \approx 0.34009$. It may be a good candidate for a cage-formation ground state, drawing the analogy to my 2D observation for the honeycomb lattice, see Section VIII D. If my geometric-ground-state framework turns out to have merit in 3D and the diamond lattice can indeed influence the fluid, this effect should already be present for unexpectedly low volume fractions. It would therefore be interesting to see what experiments similar to the ones in Ref. [2] would reveal in a 3D system.

There is one final possibility for generating uniform Voronoi cells that I could find, namely to use a tetrahedral-octahedral honeycomb. In this arrangement, the particles are the inscribed spheres to the octahedra comprising the honeycomb and each of the two tetrahedra to an octahedron contributes 1/4 of its volume to the Voronoi cell. This gives the volume fraction $\eta = 8\pi/(27\sqrt{3}) \approx 0.537422$, which is clearly not close to the glass transition in 3D. However, as indicated in the main text, it is close to where the random-loose packing value for a frictional hard-sphere system is placed in the literature.

Concluding, I appreciate that 3D systems are significantly more complex in terms of their geometry than 2D ones. In my brief analysis of plesiohedra and tilings, I was unable to identify a particularly good candidate geometric ground state that could match η_g . This does not mean that there are no effects in 3D and it does not mean to imply that the glass transition in 3D needs to be understood in this framework. Further work is clearly required in this direction before any definitive conclusions can be drawn.